DIPLOMARBEIT

Localization of MHD modes in the pedestal of ASDEX Upgrade

Ausgeführt am

Max-Planck-Institut für Plasmaphysik

unter Anleitung von

Prof. Elisabeth Wolfrum

Vienna, 13th December, 2021

Markus Wappl

Abstract

In the inter-ELM phase of H-mode plasmas at ASDEX Upgrade, MHD modes appear in the magnetic signature. They exhibit a frequency range up to several hundred kHz and can be observed through pick-up coils. This thesis aims to localize their radial position in the plasma as well as to find the velocity with which they move to compare it to plasma drifts.

Possible driving causes for the modes follow from a TOKAMAK stability consideration. An overview of mode types is given. The mode structure is characterized by two parameters, the poloidal mode number m and the toroidal mode number n. It is discussed how the magnetic topology, especially the safety factor, determines the mode structure. This relation to the safety factor presents a possibility to localize the modes. The applied diagnostics are presented and a program to compute the mode numbers is explained. This includes a new subroutine for the determination of the poloidal mode number. Calculation of diamagnetic drift velocities was done in a recent bachelor's thesis through a novel fitting routine, which is also explained.

Based on several examples from the type-I ELM regime, the localization and velocity calculation is demonstrated. The localization consistently yields a position close to the separatrix, the precision is ultimately limited by the range of the equilibrium reconstruction. A clear discrepancy in the velocity compared to plasma drifts is shown which hints at the presence of a wave phenomenon adding a phase velocity.

Kurzfassung

In der inter-ELM Phase sogenannter H-Moden Plasmen am ASDEX Upgrade TOKAMAK erscheinen MHD-Moden in der Magnetik. Sie haben einen Frequenzbereich bis zu mehreren hundert kHz und können mittels Induktionsspulen beobachtet werden. Ziel dieser Arbeit ist deren radiale Lokalisierung im Plasma sowie die Bestimmung der Geschwindigkeit der Moden, um sie mit Plasmadriften zu vergleichen.
Mögliche Auslöser und Treiber von Moden folgen aus einer Betrachtung der TOKAMAK Stabilität. Ein Überblick verschiedener Typen von Moden wird gezeigt. Die Modenstruktur ist durch zwei Parameter charakterisiert, die poloidale Modenzahl m und die toroidale Modenzahl n. Es wird diskutiert wie die magnetische Topologie, im Speziellen der Sicherheitsfaktor, verantwortlich für die Modenstruktur ist. Diese Beziehung zum Sicherheitsfaktor bietet eine Möglichkeit zur Lokalisierung der Moden. Verwendete Diagnostiken werden vorgestellt und ein Programm zur Bestimmung der Modenzahlen wird erklärt. Dies beinhaltet eine neuartige Subroutine für die poloidale Modenzahlbestimmung. Diamagnetische Driften wurden kürzlich in einer Bachelorarbeit mit einer neuen Fitroutine berechnet, die ebenfalls erklärt wird.
Anhand von einigen Beispielen aus dem Typ-I ELM Regime wird die Lokalisierung und Geschwindigkeitsberechnung demonstriert. Bei der Lokalisierung wird wiederholt eine Position nahe der Separatrix erhalten, die Präzision ist durch die Reichweite des Equilibriums limitiert. Eine eindeutige Diskrepanz zwischen der Modengeschwindigkeit und den Plasmadriften wird gezeigt, was auf ein Wellenphänomen mit zusätzlicher Phasengeschwindigkeit hindeutet.

Contents

Chapter 1

Introduction

1.1 Why fusion?

In the race for the major energy source of the future, the final word has not been spoken. The landscape of energy provision has to transform in order to sustain the development of humanity. From the year 1999 to 2019, the worldwide primary energy consumption has increased by 52 %. [1] While the COVID-19 pandemic has curbed economic growth and energy demand on a global level, the long-term trend is thought to continue. At the same time, an important goal is to reduce the emission of greenhouse gases, foremost carbon dioxide, which is proven to be the driving cause of the current global warming. [2]

Burning fossil fuels has been a dependable energy source for decades. In 2019, still over 80 % of all primary energy consumption was covered by combustion, mostly of fossils. [1] Its fault lies in the release of carbon from the earth's crust into the atmosphere. Also, the availability of these resources on the planet is ultimately limited.

There is anticipation of so-called renewable energy sources. These are supposed to stay available without the need for vanishing resources while having no troubling impact on the environment. The term includes forms such as hydropower, wind power and solar power.

While countries like Austria can make substantial use of hydropower, this is bound to geographical conditions and not an option everywhere in the world. Additionally, the large-scale implementation of river power plants such as the Three Gorges Dam in China can have disastrous humanitarian and ecological consequences. [3]

Conventional wind power allows for sustainable generation of electricity. The drawback is the weather dependence which makes it seasonal in some regions. Only facilities in advantaged areas like offshore can effectively cover base load. This, in turn, requires very long power lines and therefore power losses. One ecological point of criticism is bird strike. [4]

There are different forms of solar energy usage. Especially photovoltaics is a field of current research and could see major efficiency improvements in the near future. [5] However, all forms of solar energy depend on direct sunlight and are restricted to daytime hours, making also them problematic for base load.
The most hotly debated option is nuclear energy, to this day only available from nuclear fission power plants. It has the advantages of large power capacity, location independence and the lack of carbon dioxide emission. The consequences of possible malfunctions in such power plants are tremendous. Even in orderly operation, the process puts out highly problematic waste whose final disposal is still unsolved. With a required isolation time in the range of a million years for contaminants [6], the issues of nuclear fission generally outweigh the benefits.
A great deal of research is devoted to devising an energy source that is dependable and powerful while it spares the environment and can be deployed everywhere. Nuclear fusion is a bearer of hope, with the upsides of nuclear fission, but without the threat of catastrophe and potentially no long-term radioactive waste.

1.2 Nuclear fusion reactions

Energy can be retrieved from nuclear reactions due to the mass defect, corresponding to the binding energy within nuclei. The relevant quantity is the binding energy E_B per constituents, which are generally called nucleons. There is an empirical relation between the mass number A of a stable nucleus and the binding energy per nucleon. A graphical representation can be seen in figure 1.1, which shows the direction of reaction that allows energy release as pink arrows. The inverse of the binding energy per nucleon $-E_\mathrm{B}/A$, measured in MeV is plotted over the mass number A. It is strictly negative and has a minimum in the nucleus of iron at $A = 56$, as indicated by a vertical, grey line. Any nucleus more massive than that can set energy free via fission. On the other hand, lighter nuclei beginning from sole protons can release energy by fusing with others. Three relevant nuclides, deuterium ^{2}D, tritium ^{3}T and helium ^{4}He, are highlighted as an orange circle, a red triangle and a blue diamond, respectively. Other nuclides appear as green hexagons in figure 1.1.

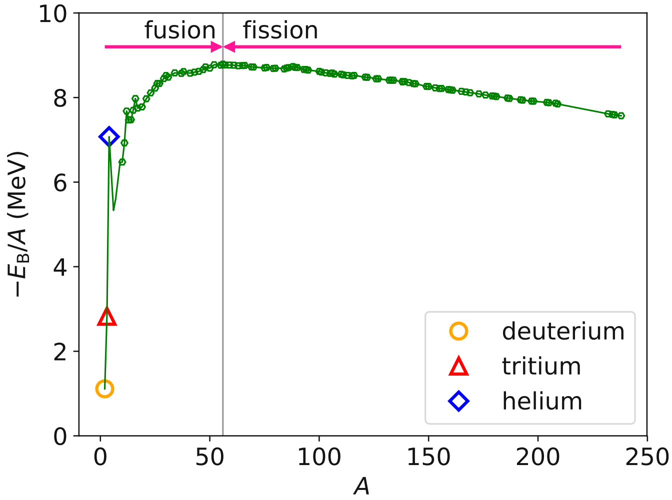

Figure 1.1: Inverse binding energy per nucleon $-E_\mathrm{B}/A$ over mass number A for selected nuclides, shown as green hexagons. An orange circle stands for deuterium ^{2}D, a red triangle for tritium ^{3}T and a blue diamond for helium ^{4}He. The vertical, grey line indicates the strongest binding at $A = 56$ for iron. The arrows in pink are directed towards binding energy release. (data from [7][8])

Most of the sun's power stems from the so-called pp-cycle. It revolves around the fusion of protons to helium nuclei amongst beta plus decay. However, the starting reaction between two protons is very slow, which makes it unfeasible for implementation.

There are numerous thinkable fusion reactions for energy provision on earth. However, they are not all equally favorable based on the availability of their reactants, interaction cross-section, or possible radioactivity of their final products. Helium, like in the pp-cycle, is a preferable product. The most straightforward reaction would be two deuterons to one helium nucleus according to equation 1.1.

$$^2\mathrm{D} + {}^2\mathrm{D} \longrightarrow {}^4\mathrm{He} + 23.8\,\mathrm{MeV} \tag{1.1}$$

Unfortunately, this three-body collision is illegal for free particles because of momentum conservation. The one nuclear reaction that is prospectively going to realize energy production is that of a deuteron and triton, like in equation 1.2.

$$^2\mathrm{D} + {}^3\mathrm{T} \longrightarrow {}^4\mathrm{He} + {}^1\mathrm{n} + 17.6\,\mathrm{MeV} \tag{1.2}$$

It satisfies momentum conservation and releases 17.6 MeV of energy in the center of mass frame. The interaction cross-section has its maximum at a center of mass frame energy of 65 keV for the reactants. [9]

Unlike in fission, this process knows no chain reaction and has a threshold energy due to the electromagnetic repulsion of the nuclei. In addition, the released energy from fusion reactions drives the reactants apart. Energy must be invested first to start the reaction, then the fusion fuel must be confined. If enough power is released, it can provide the threshold energy for a self-sustained fusion reaction. There is Lawson's criterion which formulates the physical requirements for this situation. It is shown in equation 1.3 with the particle density n, temperature T and the confinement time τ_{E}. Note that the confinement time is not the duration of confinement, but rather a time constant for the loss of stored thermal energy.

$$n \cdot T \cdot \tau_{\mathrm{E}} \geq \text{const.} \tag{1.3}$$

Several ideas have been put forward to fulfill Lawson's criterion, with only two of them possessing relevance today, magnetic confinement and inertial confinement. In the following, a closer look is taken at the TOKAMAK, one form of technical realization for magnetic confinement.

1.3 Magnetic confinement

The approach in magnetic confinement utilizes deuterium and tritium fuel at comparably low density with high thermal energy. Due to collisions at high thermal velocity, the molecules in the fuel get ionized, meaning that they break up into charged ions and electrons which can be manipulated by electric and magnetic fields. Such a fully ionized gas is called a plasma. Charged, free particles will follow magnetic field lines in a circular or spiral motion. This effect called gyration is a consequence of the Lorentz force and the foundation of magnetic confinement.

Given a particle with defined charge q and mass m, the angular frequency ω of the gyration in a magnetic field $\vec{B}$ is fixed to equation 1.4. It will couple to electromagnetic waves of the same frequency. The gyration radius is variable and changes with the kinetic energy of the particle.

$$\omega = \frac{q \cdot |\vec{B}|}{m} \tag{1.4}$$

In a simplified, classical picture, a homogeneous magnetic field inhibits charged particles from escaping in perpendicular direction to the field lines. However, the particles can freely move parallel to the field lines and therefore violate confinement in a bounded fusion device. The solution of choice is to bend the field lines to a circular shape so that they close within the fusion device and never lead particles outside. A donut-like shape, a so-called torus, is the result. One can easily see that the magnetic field is then no longer homogeneous, with higher field strength on the inside of the torus than on the outboard side. Also, the confined particles move on orbits in an accelerated motion.
A gyrating particle under the influence of an additional constant force moves with a constant drift velocity. The direction is not that of the acting force, but given by the vector product of magnetic field and force vectors. Particle drifts can be derived from the guiding center approach, which dissects the position vector in a gyration radial vector and a gyration center vector. [10] The result is the drift velocity $\vec{v}_{\mathrm{D}}$ in equation 1.5, with the acting force $\vec{F}$, the magnetic field $\vec{B}$ and the particle charge q. Note that the drift as a uniform motion is independent of particle mass, but changes with the sign of charge.

$$\vec{v}_{\mathrm{D}} = \frac{\vec{F} \times \vec{B}}{q \cdot |\vec{B}|^2} \tag{1.5}$$

The torus shape firstly dictates two extra forces, one from the gradient of the magnetic field and the other being the centripetal force based on the curvature. Both are directed to the outboard side of the torus. They cause affected particles to drift along the vertical axis, which shall be called z. Since the velocity is charge dependent, positive ions and electrons get separated and cause an electric field, also along the z-axis.
The electric field $\vec{E}$ acts as a force on charged particles and likewise creates a drift. The charge dependence of that force cancels that of the drift so that all particles drift in an equal direction, which is to the outboard side. An expression for the resulting drift velocity $\vec{v}_{\mathrm{ExB}}$ is given in equation 1.6, charge dependence is notably absent. Particles follow the direction of the initial cause to these drifts and move out of the torus. Again, a loss of confinement is the consequence.

$$\vec{v}_{\mathrm{ExB}} = \frac{\vec{E} \times \vec{B}}{|\vec{B}|^2} \tag{1.6}$$

Magnetic confinement consistent in the scope of classical effects can be achieved with a twisted magnetic field in torus shape. Such a field geometry can be thought of as a superposition of a purely toroidal field component, as described above, and one that runs along the short circumference of the torus, a poloidal component. This causes partial annihilation of the drift, averaged along a field line, and allows currents to relax the charge separation that causes the outwards drift, the so-called Pfirsch-Schlüter currents.

A helically twisted magnetic field can be produced with a complex coil geometry and is realized in machines called Stellerators. The other implementation of a torus-shaped fusion device is the TOKAMAK. It generates a toroidal magnetic field with designated coils. A central solenoid amidst the torus produces a varied magnetic flux that induces a toroidally directed current through the plasma. From this plasma current, a poloidal magnetic field arises. The overlay of toroidal and poloidal magnetic field leads to the necessary twisted field lines. Unlike a Stellerator, a TOKAMAK is toroidally symmetrical, meaning completely invariant against toroidal rotation. Due to the induction principle, TOKAMAK operation is temporally limited to pulses, which can be seen as a downside. On the other hand, the coil architecture is much simpler and the principle more elegant compared to the Stellerator. It also has an inherent ohmic plasma heating due to the current.

In magnetic confinement devices, helium nuclei as reaction products underlie confinement and exchange energy with fusion fuel, thereby heating it. Neutrons as neutral particles leave the plasma, so their energy becomes usable for electricity generation. Once fusion reactions occur at a significant rate, the so-called helium ash needs to be expelled from the plasma together with possible impurities. In most modern fusion devices, the outer layers of the plasma are directed onto a set of plates called a divertor. It absorbs the thermal energy of the impinging plasma while protecting other parts of the vessel from it. Additional field coils shape the plasma in the respective form, which will be discussed in chapter 1.4.

This thesis is based on ASDEX Upgrade, a mid-sized TOKAMAK in divertor configuration. A sectional drawing of this machine can be seen in figure 1.2. It includes the vessel and various inlet tubes in blue and grey and magnetic field coils in bronze. The plasma inside the vessel is shown as a purple glow.

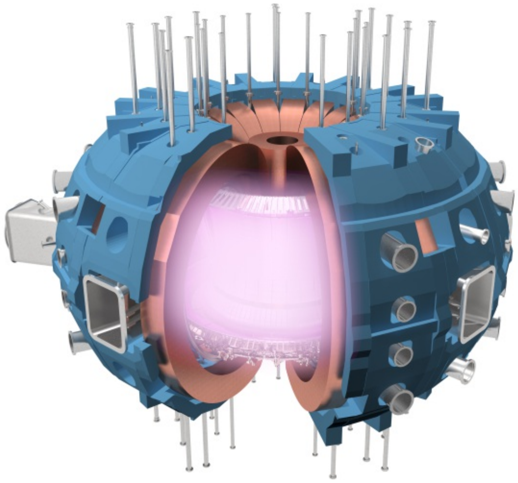

Figure 1.2: Sectional drawing of ASDEX Upgrade. There is the vessel and various inlet tubes drawn in blue and grey and magnetic field coils in bronze. The plasma inside the vessel is shown as a purple glow. (picture from [11])

1.4 Flux surfaces

A toroidal plasma consists of nested surfaces defined by constant magnetic flux ϕ, the flux surfaces. The innermost flux surface, collapsed to one dimension, is known as the magnetic axis. On the other hand, the outermost magnetic surface that still closes inside the plasma vessel is called the separatrix.
At this point, coordinates to parameterize a torus shall be introduced. Two different sets can be seen in figure 1.3. Depending on utilization, cylindrical coordinates can be chosen, including the radius R, the vertical coordinate z and the toroidal angle ϕ. The major radius R_0 denotes the distance from the central z-axis to the magnetic axis. Another coordinate system can be constructed from the minor radius r, measured from the magnetic axis, the poloidal angle θ and again the toroidal angle ϕ.

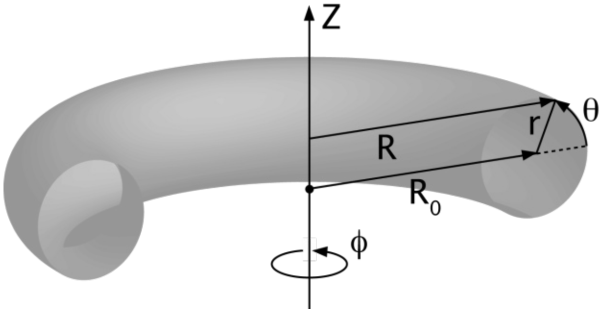

Figure 1.3: Different coordinates for a torus, including the radius R, vertical coordinate z, toroidal angle ϕ, major radius R_0, minor radius r and poloidal angle θ. (picture from [12])

Some more terms are commonly used for localities around the torus. Because of the weaker magnetic field at the previously mentioned outboard side, this is also called the low field side (LFS), as opposed to the inwards facing high field side (HFS). The plane defined by $z = z_{\mathrm{axis}}$ is called the midplane, lying parallel to ground level at the height of the magnetic axis.

In figure 1.4, a cross section through a plasma at ASDEX Upgrade is shown. It features nested flux surfaces as dashed, red lines. Those inside of the separatrix are closed, others lying outside appear to split up. The separatrix itself can be seen as a solid blue line. Surrounding vessel components are included in grey in the picture. The plasma cross section is not circular, but elongated and asymmetrical. Note that the magnetic axis is not exactly at half the vessel height, which is generally not the case.

At the bottom, the separatrix crosses itself to a so-called x-point. This is a feature of the divertor configuration. ASDEX Upgrade has a special, closed lower divertor and an open upper divertor, both visible as grey structures in figure 1.4 below and above the plasma, respectively. Field lines outside of the separatrix are directed onto the divertor where plasma flow is absorbed. The portion of the plasma outside of the separatrix is therefore called the scrape-off layer (SOL).

Instead of the minor radius r, so-called flux coordinates are often used. In the scope of this thesis, the coordinate ρ_{pol} is employed as defined in equation 1.7. It is based on the magnetic flux through a poloidally oriented surface ψ at a given location. The definition includes the magnetic flux at the separatrix ψ_{sep} and that at the magnetic axis ψ_0. This coordinate makes sense, because many quantities are constant on flux surfaces and a function of ρ_{pol}, such as the mode numbers introduced in chapter 1.5.

$$\rho_{\mathrm{pol}} = \sqrt{\frac{\psi - \psi_{\mathrm{a}}}{\psi_{\mathrm{sep}} - \psi_{\mathrm{a}}}} \tag{1.7}$$

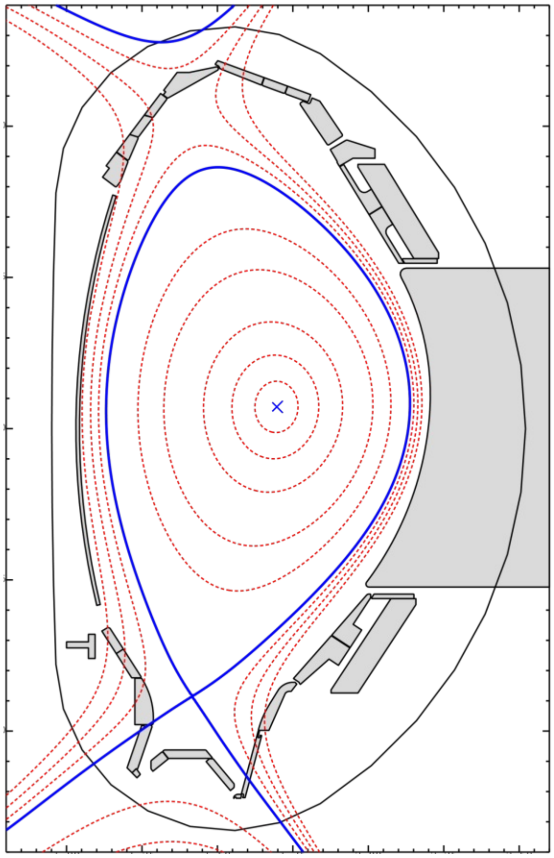

Figure 1.4: Cross section of a TOKAMAK plasma. Flux surfaces are shown as dashed, red lines, closed inside the separatrix and diverging outside. The separatrix itself appears as a solid blue line with the x-point at the bottom. Surrounding vessel components are included in grey in the picture.

The twisting of field lines can be expressed as a field line slope α as in equation 1.8 with the poloidal field component B_{pol} and the toroidal field component B_{tor}.

$$\alpha = \arctan \frac{B_{\text{pol}}}{B_{\text{tor}}} \tag{1.8}$$

The field line slope is a local variable. A related, global quantity can be defined from the revolutions of field lines around the torus, toroidally and poloidally, respectively. It is named the safety factor q, equal to the number of toroidal revolutions of a field line per poloidal revolution of the same field line. The safety factor is constant on each flux surface and can basically be any real number. In the case that a field line closes in itself after a finite number of revolutions, q takes on a rational number. Flux surfaces for which this is fulfilled are called rational surfaces. In a TOKAMAK plasma, q is a bijective function of ρ_{pol}. It is therefore possible to relate a certain radial position and flux surface in the plasma to a numeric safety factor.

Towards the separatrix, the safety factor goes to infinity. Near the plasma edge, its value is constituted mostly by the x-point seen in figure 1.4. The field line slope, for instance at the outboard midplane, is therefore very unlike the safety factor, which must be taken into account when a global quantity is defined. This is possible through an alternative poloidal coordinate, the so-called straight field line angle θ^*. Its defining property is that in the (θ^*, ϕ) basis, the field line slope is a constant of θ^* and ϕ. This leads to the self-titled straight field lines. In figure 1.5, the course of magnetic field lines is shown in the (θ, ϕ) plane in figure 1.5a and in the transformed (θ^*, ϕ) system in figure 1.5b.

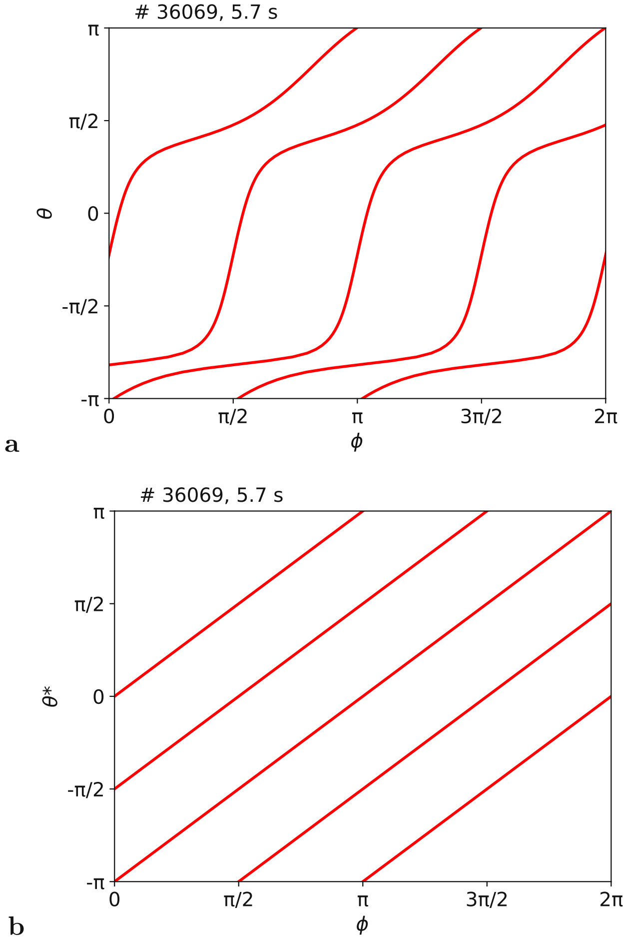

Figure 1.5: Comparison of the magnetic field line course in a) the (θ, ϕ) and b) in the (θ^*, ϕ) plane with the straight field line angle θ^*.

1.5 Phenomenology of modes

While TOKAMAK experiments already reach significant particle densities and temperatures, the remaining issue is to reach a sufficient confinement time. In addition to the classical model of the plasma, so-called neoclassical trajectories must be considered. Due to collisions, particles can transition between trajectories in a random walk. This increases transport of particles and heat out of the plasma. Moreover, research from the past decades show that in fact, TOKAMAK plasmas behave in a turbulent fashion which dominates transport. There are different types of modes in a fusion plasma, which arise from instabilities or excitations, intertwined with transport phenomena.

As the plasma particles are bound to magnetic field lines by gyration and vice versa, it is often said that the magnetic flux is frozen into the plasma. This means that any broadening or reshaping of the plasma is accompanied by a change in the magnetic field. Near the plasma edge, so-called MHD modes manifest as displacement of magnetic field lines and can be detected through inductivity.

For energetic reasons, MHD modes are restricted to rational surfaces. [13] This leads to a forced periodicity based on the closed field line structure. Different harmonics are possible, which can be characterized by two mode numbers, the poloidal mode number m and the toroidal mode number n. The mode numbers can be thought of as the numbers of maxima along a poloidal or toroidal revolution, respectively. Due to the periodic boundary conditions on rational surfaces, both mode numbers are not independent. The relation reads as equation 1.9. A mathematical motivation of the mode number concept will be given later in chapter 2.2.

$$q = \frac{m}{n} \tag{1.9}$$

As the plasma moves due to various drifts, such as $\vec{v}_{\mathrm{ExB}}$, the modes are in motion as well. Depending on what drives a mode, the drift velocity differs. Various driving causes for modes are introduced in chapter 2.3. The mode movement shows as a periodic signal with a frequency depending on the velocity and mode numbers when measured at a fixed location around the torus.

The direction of any drift in the plasma is strictly perpendicular to the magnetic field because it arises from a vector product with the magnetic field as shown in equation 1.5. The orientation of drifts with positive sign is denoted as co-current direction, the opposite is called the counter-current direction. However, other forms of motion may be observed in modes. Due to restoring forces in the displaced magnetic field or fluid pressure in the plasma, modes can wander along field lines. Such phenomena are unified under the term MHD waves and are treated in chapter 2.4.

1.6 Thesis goals

The localization of MHD modes by means of the flux coordinate ρ_{poloidal} is the primary goal of this thesis. The approach is the determination of both the poloidal mode number m and the toroidal mode number n of the same structure. Under the assumption of the locality at a rational flux surface, the safety factor q corresponds to m/n. From knowledge of the safety factor profile, owed to a high-resolution equilibrium reconstruction, the position in ρ_{pol} can be found.

The scope also includes the velocity determination of aforementioned modes. Through the quotient of frequency and mode number, the rate at which the structure passes the coils can be found. It is converted into the velocity in perpendicular direction to the local magnetic field on the outboard midplane. This can be compared to the drift velocities in the plasma.

Drift velocity profiles over ρ_{pol} are determined from measured profiles. If agreement between the mode velocity and the drift at the ascertained position is found, this acts as a double-check for the localization.

In the next chapter, a glimpse into the underlying MHD equations is taken. A lot of the terminology in plasma edge physics is explained in more depth. The different types of expected MHD modes are characterized.

The third chapter lists all the plasma diagnostics that provide important data for the analyses in the thesis. Short descriptions of their functioning principle and peculiarities are given.

Chapter four deals with the computation of mode numbers. This is done with a dedicated program originally devised by Felician Mink and adapted for this thesis. [14] The details of its functionality are explained and visualized. Sources of error and further processing of the results are shown.

In the fifth chapter, the results of the localization and velocity calculation for selected discharges are presented. It is shown how the results contradict previous conceptions about the nature of the modes. Possible explanations are discussed.

The last chapter gives a short summary and outlook on future research.

Chapter 2

MHD description of TOKAMAK plasmas

The behaviour of a plasma under the influence of magnetic and electric fields is described by the theory of magnetohydrodynamics, shortly referred to as MHD. It treats plasma as a many-body, multi-species fluid and attributes typical fluid properties such as density, temperature and pressure to it.
To derive a closed set of equations of MHD, the system is first simplified to a one-species fluid. In the scope of this thesis, it is justified by the overwhelming abundance of deuterium ions ($Z = 1$) compared to other species in the plasma and the fact that electrons yield nearly no contribution to the mass density. The terms ion fluid and electron fluid are used in the following for these separate but interacting subsystems. The following equations 2.1 to 2.14 stem from the book "Magnetohydrodynamic Stability of Tokamaks" by Hartmut Zohm. [13]
A defining property of plasma is quasi-neutrality, meaning equal ion and electron particle densities $n_i = n_e = n$ for a $Z = 1$ plasma. Through intra-species collisions of ions and electrons, the plasma can become thermalized and gain a defined ion temperature T_i and electron temperature T_e. These two quantities do not have to coincide. The mass density ρ_m reads as equation 2.1.

$$\rho_\mathrm{m} = n_\mathrm{i} \cdot m_\mathrm{i} + n_\mathrm{e} \cdot m_\mathrm{e} \approx n \cdot m_\mathrm{i} \tag{2.1}$$

Also the center of mass velocity $\vec{v}$ is dominated by the ion fluid velocity $\vec{u}_\mathrm{i}$, seen in equation 2.2.

$$\vec{v} = \frac{1}{\rho_\mathrm{m}}(n \cdot m_\mathrm{i} \cdot \vec{u}_\mathrm{i} + n \cdot m_\mathrm{e} \cdot \vec{u}_\mathrm{e}) \approx \vec{u}_\mathrm{i} \tag{2.2}$$

The electrons do, however, contribute to the current density according to equation 2.3.

$$\vec{j} = e \cdot n(\vec{u}_\mathrm{i} - \vec{u}_\mathrm{e}) \tag{2.3}$$

By describing the plasma as a gas of free particles, also a pressure can be defined according to the ideal gas law, comprised of an ion fluid contribution and an electron fluid contribution, as seen in 2.4.

$$p = p_\mathrm{i} + p_\mathrm{e} = n \cdot k_\mathrm{B}(T_\mathrm{i} + T_\mathrm{e}) \tag{2.4}$$

Based on these quantities, MHD equations are formulated. There is the continuity equation of mass density, equation 2.5.

$$\frac{\partial \rho_\mathrm{m}}{\partial t} + \vec{\nabla} \cdot (\rho_\mathrm{m} \vec{v}) = 0 \tag{2.5}$$

Continuity must also hold for the charge density ρ_el. Quasi-neutrality commands the charge density to be zero, so the result is the vanishing divergence of the current density $\vec{j}$ in equation 2.6.

$$\vec{\nabla} \cdot \vec{j} = 0 \tag{2.6}$$

A force balance equation for the mass density is given in equation 2.7, where D denotes the substantial derivative. It includes a diamagnetic term based on the pressure gradient $\vec{\nabla} p$ and the Lorentz force. The contribution of the electric field for ions and electrons evens out here.

$$\rho_\mathrm{m} \frac{\mathrm{D}\vec{v}}{\mathrm{D}t} = -\vec{\nabla} p + \vec{j} \times \vec{B} \tag{2.7}$$

The motion of the electron fluid is described by Ohm's law in equation 2.8.

$$\vec{E} + \vec{v} \times \vec{B} = \eta \vec{j} + \frac{1}{e \cdot n}(\vec{j} \times \vec{B} - \vec{\nabla} p_\mathrm{e}) - \frac{m_\mathrm{e}}{e} \frac{\partial \vec{u_\mathrm{e}}}{\partial t} \tag{2.8}$$

Maxwell's equations read as equation 2.9 to 2.12 in the context of a plasma.

$$\vec{\nabla} \cdot \vec{E} = 0 \tag{2.9}$$

$$\vec{\nabla} \cdot \vec{B} = 0 \tag{2.10}$$

$$\vec{\nabla} \times \vec{E} = -\frac{\partial \vec{B}}{\partial t} \tag{2.11}$$

$$\vec{\nabla} \times \vec{B} = \mu_0 \cdot \vec{j} + \epsilon_0 \mu_0 \cdot \frac{\partial \vec{E}}{\partial t} \tag{2.12}$$

Lastly, the pressure shall be related to the mass density through an adiabatic index γ_a, like in equation 2.13.

$$\frac{d}{dt}\left(\frac{p}{\rho_\mathrm{m}^{\gamma_\mathrm{a}}}\right) = 0 \tag{2.13}$$

In an equilibrium, partial time derivatives in a force balance like equation 2.7 shall vanish. MHD equilibria are therefore characterized by equation 2.14.

$$\vec{\nabla} p = \vec{j} \times \vec{B} \tag{2.14}$$

The closed set of equations 2.5 to 2.13 may be simplified under specific assumptions. In fusion plasmas, the Ohmic resistivity η and inertia of electron mass m_e is mostly negligible. Eliminating them leads to the ideal MHD equations.
For a toroidally symmetrical plasma with a stationary toroidal magnetic field B_tor like in a TOKAMAK, the system can be further simplified to the reduced MHD equations. Without giving details on the derivation here, an equilibrium in a TOKAMAK fulfills the Grad-Shafranov equation 2.15. [14] It is crucial for reconstructing the magnetic field structure in TOKAMAK operation.

$$R\frac{\partial}{\partial R}\left(\frac{1}{R}\frac{\partial\psi}{\partial R}\right)+\frac{\partial^2\psi}{\partial z^2}+\mu_0(2\pi R)^2\frac{\mathrm{d}p}{\mathrm{d}\psi}+(2\pi)^2 RB_\phi\frac{\mathrm{d}(RB_\phi)}{\mathrm{d}\psi}=0 \tag{2.15}$$

2.1 Formation of the Edge transport barrier

Upon overcoming a threshold of heating power, a TOKAMAK plasma can switch into the so-called H-mode (high confinement mode) as opposed to the L-mode(low confinement mode). [15] In this operational scenario, a radial electric field, in the direction of the minor radius r, is formed, accompanied by a strong velocity shear. The exact causality of which comes first is still being researched, but the relation between electric field and velocity follows from the treatment of drift velocities in chapter 1.3.
The velocity shear can be understood as different radial layers of the plasma near the plasma edge moving at different velocities, which has consequences for transport over the plasma edge. Turbulence, which is the driving cause of transport in L-mode, manifests in vortices near the plasma edge, also known as eddies. In H-mode, turbulence is strongly suppressed, lowering ion transport nearly to neo-classical expectations. There are contrasting images to how exactly the suppression happens, either by decorrelation of the turbulent eddies or rather by thinning of vortices to the point that they no longer carry radial transport. Either way, the velocity shear appears to form a barrier against transport just inside of the plasma edge, known as the edge transport barrier or ETB. [16]
Large gradients of particle density, temperature or resulting pressure could normally not form as transport would relax them. The ETB allows a steepening of these quantities in a narrow layer at the edge of the plasma. An example for such a pressure profile is shown in figure 2.1. It features its steepest gradient between $\rho_\mathrm{pol} = 0.98$ and 1. The name given to the area of increased gradients is pedestal.

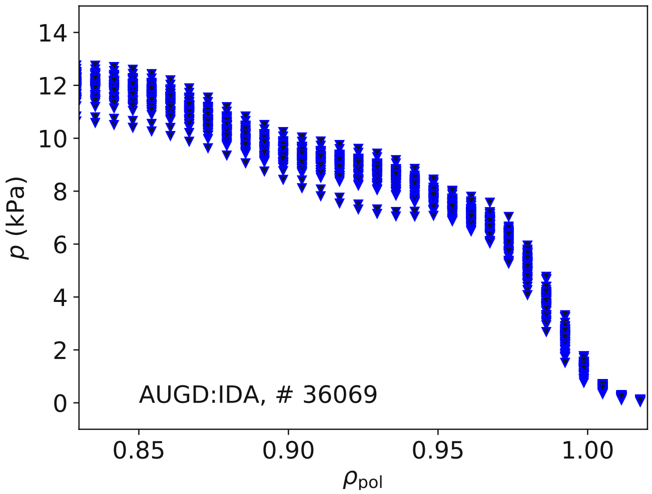

Figure 2.1: Radial electron pressure profile near the plasma edge. The region with the steepest gradient is called the pedestal.

A pressure gradient acts a force that gives rise to another drift, the diamagnetic drift. It depends on the particle charge q and is separated in ion respectively electron diamagnetic drift. Electrons drift parallel to the drift based on the radial electric field, positive ions in antiparallel direction. Accordingly, these directions are termed electron diamagnetic and ion diamagnetic direction. The drift velocity expression is given in equation 2.16.

$$\vec{v}_{\mathrm{dia}} = \frac{\vec{\nabla} p \times \vec{B}}{qn|\vec{B}|^2} \tag{2.16}$$

The H-mode is an important discovery as it can substantially improve confinement in fusion plasmas. However, the increased energy stored inside of the pedestal poses a threat to plasma-facing components if released. The edge transport barrier can be briefly broken down by an edge localized mode or ELM. Such events are observed periodically in H-mode and will be discussed in chapter 2.2.

2.2 MHD stability and the ELM cycle

A plasma in an equilibrium situation is not necessarily stable against deviations. To investigate the stability of a system without fully solving the underlying equations, a linearization is often instructive. The following deduction is again based on [13]. Quantities Q are written as the sum of their equilibrium value Q_0 and first order deviation Q_1, like equation 2.17.

$$Q = Q_0 + Q_1 \tag{2.17}$$

The velocity deviation is defined as the time derivative of a displacement vector $\vec{\xi}$, while the equilibrium value is zero.

$$\vec{v} = \cancel{\vec{v}_0} + \vec{v}_1 = \frac{\partial \vec{\xi}}{\partial t} \tag{2.18}$$

With this, the non-stationary force balance equation 2.7 becomes the equation of motion for the displacement 2.19, simplified to a linear force operator $\hat{\mathrm{F}}$.

$$\rho_\mathrm{m} \frac{\partial^2 \vec{\xi}}{\partial t^2} = \hat{\mathrm{F}} \vec{\xi} \tag{2.19}$$

Equation 2.19 is solved by $\vec{\xi}(t) = \vec{\xi}_0 \cdot e^{-i\omega t}$. For a real ω, the solution is a stable oscillation. However, for an imaginary ω with $\omega^2 < 0$, the deviation grows exponentially. This reflects a case in which perturbations lead to a loss of confinement.

The separated, time independent part of the displacement can be decomposed in the (θ^*, ϕ) system. Equation 2.20 shows the explicit form, with the mode numbers m and n giving the periodicity in the exponent. It is energetically most favorable for instabilities to appear at rational surfaces where the safety factor equals the quotient of m and n.

$$\vec{\xi}_0(r, \theta^*, \phi) = \sum_{m,n} \vec{\xi}_{m,n}(r) \cdot e^{-i(m\theta^* + n\phi)} \tag{2.20}$$

To identify the sources of instability in the force operator $\hat{\mathrm{F}}$, equation 2.19 is integrated with the complex conjugated displacement $\vec{\xi}^*$ to yield δW in equation 2.21. It gives the energy gain to the system caused by the displacement.

$$\delta W = -\frac{1}{2} \int \vec{\xi}^* \cdot \hat{\mathrm{F}} \vec{\xi} \cdot \mathrm{d}V \tag{2.21}$$

Five terms follow from the operation, which are not written explicitly here for simplicity. The first three of those are strictly positive and therefore only stabilize the plasma. Any negative contribution to δW acts in a destabilizing way. The first potentially negative term depends on the inner product of pressure gradient $\vec{\nabla} p_0$ and field line curvature κ. The pressure gradient points against minor radius direction in an equilibrium and is therefore negative in (r, θ, ϕ)

coordinates. On the other hand, the curvature is positive on the high field side and negative on the low field side in the same coordinate system. The pressure causes instabilities on the low field side of the torus, where an outwards plasma expansion is energetically favourable. They are known as a pressure driven instabilities or, because of their expanding nature, ballooning instabilities. On the high field side, the same effect is stabilizing.

There is another term with negative sign, proportional to the current density in field direction $\vec{j}_{0\parallel}$. Its effect are current driven instabilities. Instead of expanding, these instabilities release energy by kinking of field lines, which causes the plasma edge to peel off. This explains their other naming as peeling instabilities.

In an H-mode plasma, the aforementioned modes can impair confinement to the point of a complete breakdown of the ETB. Such an event is known as an ELM or more specifically an ELM crash. A portion of energy and particle density is lost from the plasma edge, which not only disrupts confinement, but can also damage elements of the plasma vessel. Consequently, the pressure gradient as well as the current density are greatly reduced after an ELM crash. The instabilities thereby loose their driving cause so that the plasma regains stability. Due to the heating power, an ETB is restored.

The ELM returns in cycles which are characterized by an ELM frequency and different phases within one period. [17] The whole cycle lasts, depending on operational parameters, from milliseconds to some ten milliseconds. Different types of ELMs are discerned, for instance the type-I ELM cycle with a low frequency and large crashes. The modes treated in this thesis occur in the type-I ELM cycle in the inter- or pre-ELM phase, the last phase after the restoring of the pedestal leading right up to the ELM crash.

The peeling-ballooning model is an explanation for the ELM cycle. It states that only the combination of peeling and ballooning instabilities can cause an ELM crash to happen. The pressure gradient first reaches a critical limit at which not yet identified instabilities increase transport and stop the gradient from growing further. In this state, the pedestal width increases until the peeling ballooning mode is unstable and causes a major transport event. [18][19][20]

As it is derived from linear MHD, the peeling-ballooning model has limited applicability and must be supplemented by non-linear theories in some cases. Indeed, peeling-ballooning cannot explain every characteristic of the ELM cycle known experimentally. [20]

2.3 Mode types in the pedestal

In between ELM crashes, different types of instabilities can be formed. Some act as precursors to an ELM and are thought to be responsible for triggering a crash. [21] However, another important role of modes near the plasma edge is driving transport in the inter-ELM phase. This limits the achievable edge gradients such as that of the pressure. ELM crashes depend on critical limits, therefore instabilities can delay the crash, affect the length of ELM cycles and play a role in possible ELM-free scenarios. Here, a few different types of modes shall be discussed.

2.3.1 Ideal ballooning modes

This type of modes is already introduced in the peeling-ballooning model. It is driven by the pressure gradient and moves with the plasma velocity from equation 1.6 caused by the radial electric field. [21] However, according to another source based on the simulation code JOREK, the poloidal velocity of these modes is the plasma velocity plus half the ion diamagnetic velocity in equation 2.16, in addition to the projection of a parallel velocity. [22] Such a velocity parallel to the magnetic field is associated with MHD waves, which are treated in chapter 2.4.

A plasma under ideal conditions suppresses any magnetic displacement with compensation currents. At the location of an ideal mode, where the displacement $\vec{\xi}$ is at a maximum, there is hence no magnetic displacement. The measured position depends on magnetic signals and can therefore differ. [23]

2.3.2 Ideal peeling modes

Peeling modes are driven by currents near the plasma edge. Their propagation is also the plasma velocity from the electric field. [21] They suffer from the same position measurement offset as ideal ballooning modes. [23]

2.3.3 Resistive ballooning modes

Adding a finite electrical resistivity to the physical picture of the plasma gives rise to further mode types. The resistivity in a plasma follows the temperature dependency in equation 2.22, therefore it plays a role at the outer layers of the plasma where temperatures are low. [24]

$$\eta \sim T^{-3/2} \tag{2.22}$$

A resistive plasma can not perfectly compensate magnetic displacement, resistive modes are thus measured at their actual position. The type of resistive ballooning mode moves with the plasma velocity v_{ExB}. [21] Again, there is another source based on the JOREK code, which finds a poloidal velocity of v_{ExB} plus the projection of a parallel velocity. This would imply a velocity difference between ideal and resistive ballooning modes. [22]

2.3.4 Electron temperature gradient modes

The dependence on the electron temperature profile means that these modes move with the electron diamagnetic velocity and direction. They are considered to be micro-instabilities due to their large wave vector and high frequency. [21]

2.3.5 Microtearing modes

Tearing modes are anomalies, or tears, in the magnetic field line structure. Such structures are frozen into the electron fluid and therefore also move with the electron diamagnetic velocity. Magnetic islands can be formed, which are closed field lines at a small scale. Figure 2.2 gives an example with field lines drawn in red. This illustrates the concept, however tearing modes can exist in other non-homogeneous magnetic arrangements.

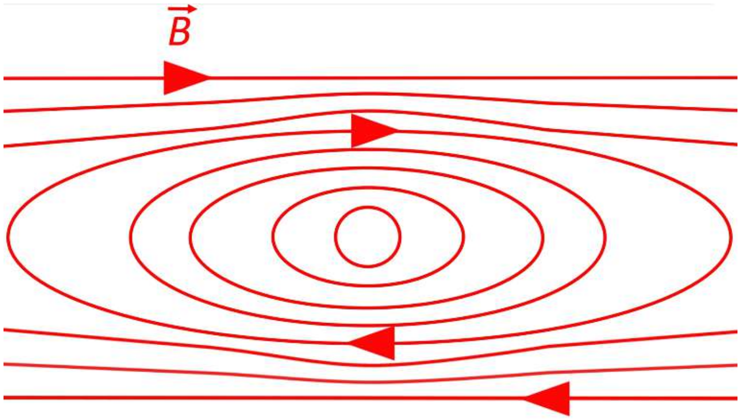

Figure 2.2: Illustration of a tearing mode with closed field lines, a magnetic island. Magnetic field lines are drawn in red.

Microtearing modes are micro-instabilities, characterized by a wave vector smaller than in electron temperature gradient modes and high frequency. [21]

2.4 MHD waves

In the scope of ideal MHD, displacement of field lines causes wave phenomena, the so-called Alfvén waves. In contrast to the previously described modes, these waves can progress along, meaning parallel to, magnetic field lines.

Any harmonic wave takes a linear restoring force to propagate. In the case of MHD waves, it can be derived from the equilibrium equation 2.14. Identifying the current density and using Ampere's law for it leads to equation 2.23.

$$\vec{\nabla} p = \vec{j} \times \vec{B} = \frac{1}{\mu_0}\left(\vec{\nabla} \times \vec{B}\right) \times \vec{B} = -\vec{\nabla}\frac{B^2}{2\mu_0} + \frac{1}{\mu_0}\left(\vec{B} \cdot \vec{\nabla}\right)\vec{B} \tag{2.23}$$

The first term in the final expression of equation 2.23 is also known as the magnetic pressure. It resists the compression of field lines. In the second term, the inner product of magnetic field and its gradient accounts for the field line curvature. The resulting so-called field line tension acts to straighten curved field lines. [13]

Two types of waves are described by equation 2.23, the compressional Alfvén waves caused by the magnetic pressure and the shear Alfvén waves that stem from the field line tension. Both these Alfvén wave types move parallel to the magnetic field. Sound waves can occur in a plasma like in a neutral gas as oscillations of the kinetic pressure p. In conjunction with a magnetic field, they lead to so-called magnetosonic waves, the third type of MHD wave. They can propagate in a direction independent of the magnetic field. [25]

The group velocity of Alfvén waves is called the Alfvén velocity v_A as seen in equation 2.24. [26]

$$v_\mathrm{A} = \frac{B}{\sqrt{\mu_0 \rho}} \tag{2.24}$$

Being a moving displacement of the magnetic field, an MHD wave can be picked up by magnetic diagnostics just as MHD modes. However, relation 1.9 for the safety factor generally does not hold. Instead, an offset can occur, for instance $q = (2m + 1)/2n$. The resulting frequency as detected by pick-up coils is the Alfvén frequency f_A. When entering the relation for q stated above, equation 2.25 follows. [26]

$$f_\mathrm{A} = \left| \frac{v_\mathrm{A}}{2\pi R} \frac{m - nq}{q} \right| = \left| \frac{v_\mathrm{A}}{2\pi R} \frac{1}{2q} \right| \tag{2.25}$$

2.5 State of MHD mode understanding

As of the beginning of this thesis, a phenomenon of high frequency modes appearing during the inter ELM phase is known. They display toroidal mode numbers of between $n = 1$ and 10 and move in the electron diamagnetic direction. Modes typically align in straight lines of constant frequency over mode number (f/n) quotients. The logical conclusion is that they move at the same velocity, which implies an origin at the same flux surface. Such a mode structure is called a branch, it describes a composition of harmonic oscillations with a shared origin. The f/n relation can be linearly fitted with a pass through the $f = 0$, $n = 0$ origin. Several branches with individual slope and overlapping mode numbers may appear at the same time. [14]

The modes are thought to be pressure driven in nature. Because of that and their appearance late in the ELM cycle, when the edge pressure gradient is readily built up, the suspicion is that these modes sit at the position of the steepest electron pressure gradient.

If an according branch with poloidal mode numbers and constant f/m could be identified, the localization would be simple through m/n. However, the calculation of poloidal mode numbers is more intricate and requires additional input, as explained in section 4.1.2. Furthermore, the result often shows a less straight-forward structure compared to n. While the modes corresponding to the n calculation can be found at the same frequencies, they might not show the same lineup in branches. Sometimes modes are aligned, but with no pass through the $f = 0$, $m = 0$ origin and therefore no constant f/m relation. Also, coherent branches in the n spectrum can be broken up into several linear m lineups with parallel shifts between them.

It is therefore necessary to develop a more derived physical picture of these modes to localize them.

Chapter 3

Plasma diagnostics

Different systems called diagnostics exploit various physical effects to extract information about the condition of the plasma. An overview of the diagnostics that are relevant for the mode number determination as well as for the calculation of flux surface and velocity profiles is given below.

3.1 Pick-up coils

There is a number of different pick-up coils installed around the ASDEX Upgrade TOKAMAK. They are divided into different arrays for distinct purposes. This thesis utilizes two coil arrays, one is spread in poloidal direction at a single toroidal position, the other one is toroidally spread on the outboard midplane. Since they are scanning for phenomena near the plasma edge such as ballooning modes, they are known as the poloidal ballooning array and the toroidal ballooning array. A depiction of the localities of these coils is given in figure 3.1, with a poloidal section through ASDEX Upgrade and the poloidal ballooning array in figure 3.1a and a toroidal section and the toroidal ballooning array in figure 3.1b. [27]

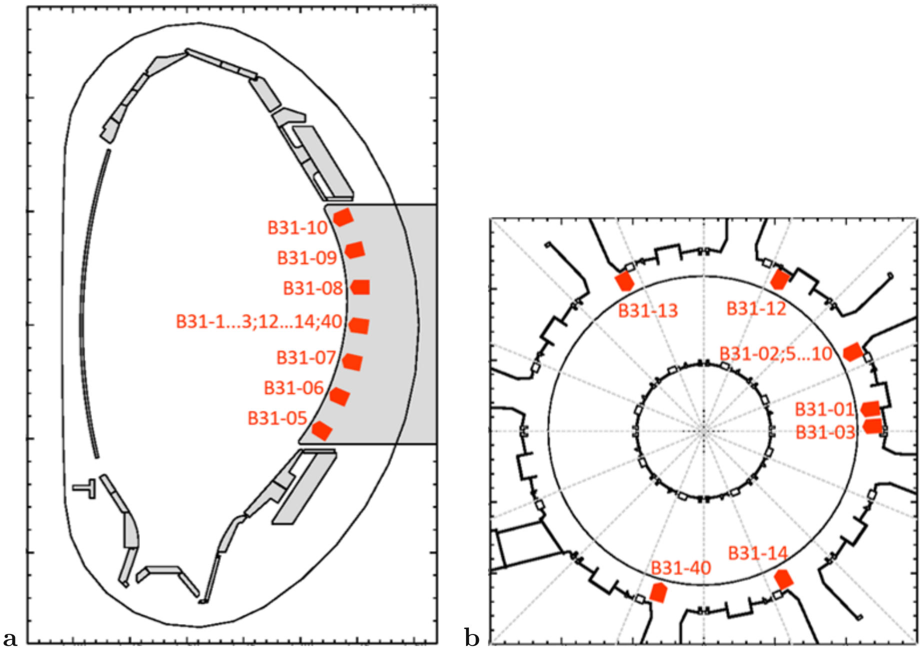

Figure 3.1: Distribution of a) the poloidal balloning coil array in a poloidal section and b) the toroidal ballooning coil array in a toroidal section of ASDEX Upgrade.

All these coils inductively detect MHD modes as temporally changing deviations from the equilibrium. In the mentioned arrays, the coil axes are pointed in minor radius direction, in which the magnetic field component vanishes in an equilibrium. The raw signal of each coil is therefore the induced voltage due to the change of radial magnetic flux at the respective coil position. Intensity, frequency and relative phase between coils can be retrieved from the signals. An example for the toroidal ballooning array coil B31-14 is shown in figure 3.2, with the time derivative of the radial magnetic field in arbitrary units over time.

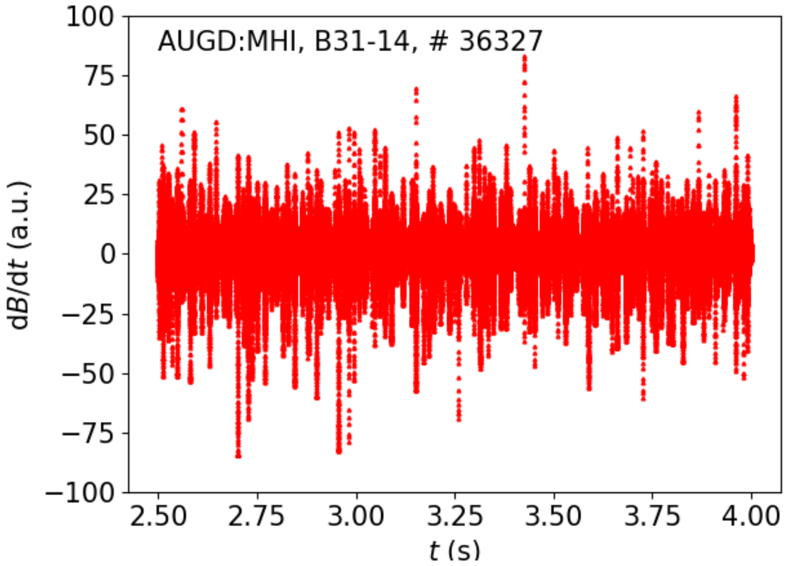

Figure 3.2: Raw signal of AUGD:MHI, B31-14, #36327. The time derivative of the radial magnetic field, proportional to the induced voltage signal of the coil is plotted in arbitrary units over time.

The further processing of each signal is explained in chapter 4.1.

3.2 Charge exchange recombination spectroscopy

Fusion experiments like ASDEX Upgrade utilize plasma heating via the injection of a neutral deuterium beam. This allows to probe temperature and drift of impurity ions. In the process called charge exchange, an electron is transferred from the neutral deuterium atom D to a positive ion I of a different sort. The ion generally adopts an excited energy state, denoted with *. A deexcitation with emission of characteristic radiation γ follows. The whole process is written down in equation 3.1. [28]

$$\mathrm{D} + \mathrm{I}^{Z+} \longrightarrow \mathrm{D}^{+} + \mathrm{I}^{(Z-1)+*} \longrightarrow \mathrm{D}^{+} + \mathrm{I}^{(Z-1)+} + \gamma \tag{3.1}$$

Spectroscopy of the characteristic radiation yields a Doppler-broadened peak. If the impurity ions possess a thermal velocity distribution, it can be fitted with a Maxwell-Boltzmann distribution. Its width accounts for the temperature of the impurities, the position of its maximum gives the drift velocity. As the emitting particles are ions, the drift is the sum of the plasma velocity and the impurity ion diamagnetic drift, which have opposing signs in the pedestal.

The interest lies not in the temperature and drift of impurities, but in that of the main plasma ions. The assumtion that impurity ions are thermalized with the same temperature as the main ions is usually fair, note however, that drift velocities depend on the charge of drifting particles. The charge state of plasma impurities depending on the abundance of various elements is unified under the effective number Z_{eff}. It tells how the impurities drift on average.
The charge cancels out for the plasma velocity in equation 1.6, but it affects the ion diamagnetic drift from equation 2.16.

3.3 Thomson scattering

An electromagnetic wave interacts with free, charged particles. The particles get excited to a harmonic oscillation following the electric field and emit an electromagnetic wave that interferes with the incident wave. This can equally be viewed as a scattering of the wave. For elastic scattering at low energies, where the particle recoil can be neglected, the phenomenon is known as Thomson scattering. In plasma physics, it is an important diagnostic tool.
The electron fluid in a fusion plasma forms a scattering medium. The intensity of the scattered radiation is proportional to the number of scattering events which translates to the electron density n. For scattering on moving particles, a Doppler shift occurs. With sufficient intensity, the spectrum of the scattered radiation reflects the velocity distribution in the electron fluid. Assuming that it is thermalized, the electron temperature T_e can be computed from the width of the spectrum. If both quantities n and T_e are known, the electron pressure p_e can be calculated with equation 2.4, together with its gradient and the resulting drift velocity.
At ASDEX Upgrade, there are two lasers that send out pulses for Thomson scattering. Both are directed vertically in z direction. One of them probes through the core of the plasma while the other one examines the plasma near the edge. The scattered radiation is measured at different positions to give a temporal and spatial resolution of the Thomson scattering signals. [29] Through identification of flux surfaces, it is possible to infer the measured quantities in other locations inside the separatrix such as at the midplane.
The localization of the measured profiles can suffer from an offset. The so-called two point model gives a hint to where a profile correctly belongs. In accordance, fitted Thomson scattering data are often shifted to match the position of $T_\mathrm{e} = 100\,\mathrm{keV}$ with the separatrix. The velocity profiles presented in this thesis were created in consideration of the two-point model. [30]

3.4 Electron cyclotron emission

The gyrating electrons emit a cyclotron radiation at harmonics of their cyclotron frequency from equation 1.4. Its dependence on the field B hints to the position of its origin in the plasma. With the input of the magnetic field distribution from an equilibrium reconstruction, the source can be localized.

The one quantity that can be deduced from the cyclotron radiation is the electron temperature. ECE can yield a profile of temperature over flux surface, or radial position, like Thomson scattering. The optical properties of the plasma are relevant. In the case that the plasma is highly absorbing to cyclotron radiation, it radiates like a black body. This leads to a direct relation between intensity and electron temperature. No particle density information can be gathered from ECE since radiation intensity only accounts for temperature in this case.

The density, in turn, affects the transparency of the plasma. In the case of a transparent plasma, the temperature determination must account for this in forward modeling.

The crucial advantage of ECE is the high sample rate, which is up to 1 MHz at ASDEX Upgrade. This ensures a faster reaction to change in the profile than for instance in the Thomson scattering diagnostic. [31]

3.5 Integrated data analysis

The integrated data analysis IDA is a computational diagnostic that unifies input from several diagnostics including Thomson scattering and ECE. Information from the different sources is merged in the frame of Bayesian statistics. [21] This enables trustworthy results with good resilience against errors from individual diagnostics. IDA produces radial profiles of electron density and electron temperature as well quantities derived from that. The standard sample rate is set to 1 kHz. [32]

3.6 Electric field evaluation

It is not possible to measure the radial electric field at the plasma edge directly. To deduce it, the movement of charged particles under its influence can be used. The EER diagnostic uses data from CXRS to set up a force balance equation for the ion fluid and reconstruct the electric field E_r. It is a computational diagnostic like IDA. The sample rate can be varied. To increase confidence, data may be averaged over ELMs. This can be problematic because the magnitude of the electric field changes throughout the ELM cycle and the result might not correspond to the desired time window. The EER data in graphs within this thesis are not averaged.

3.7 Singly charged helium spectroscopy

Neutral helium atoms are injected into the plasma for diagnostic purposes. Through inelastic collisions, they get fully ionized when reaching a thermal equilibrium. Close to the separatrix, where the energy density is not very high, these atoms can become ionized to He^1+, which has electronic states equivalent to hydrogen. Characteristic light of He^1+ is observed and its velocity distribution is obtained from the Doppler shift of the characteristic lines. The drift velocity helps to set up a force balance to find the electric field, the respective diagnostic is abbreviated as HES. Due to the helium ions in that state being non-thermalized, ion temperatures for electric field calculation must be added in from other diagnostics like CXRS.

3.8 Integrated data equilibrium

Different diagnostics as well as the knowledge of flux surface structure and magnetic field rely on a reconstruction of the magnetic equilibrium. It is calculated by numerical solving of the Grad-Shafranov equation 2.15. The integrated data equilibrium IDE is an advanced reconstruction with a sampling rate of 200 Hz. Its radial resolution is comprised by 257 data points. The outermost closed flux surface included lies at $\rho_{\mathrm{pol}} = 0.995$. This allows to access a precise safety factor close to the plasma edge. [33]

Chapter 4

Method

The determination of mode numbers based on magnetic signals is an automated process. It was originally implemented in the program `mode_determination.py` by Felician Mink in the course of his dissertation. [14] An adaptation for a python 3 environment followed in September 2020 by Markus Roth. Further expansions including a routine for the poloidal mode number determination were added during the making of this thesis. The program flow shall be explained in the following.

4.1 Mode determination program

Since a specific phase in the ELM cycle before the crash is of interest, the signals must get chopped to respective time windows, a process in the following referred to as ELM synchronization. Because the ELM crashes are visible in the coil signals as large amplitudes, flank triggering is used to determine the exact time point of each crash as the most precise method. The ELM synchronization is then performed according to times relative to the ELM crash. [14]

From the signal time traces of each coil, numeric Fourier transforms (FFT) are calculated. The FFT relies on partition into time windows.

In `mode_determination.py`, these windows are identical to the time windows that emerge in ELM synchronization. This means that a Fourier transform is calculated for each detected ELM cycle. It is possible to map the result to a histogram of intensity over frequency component and time. A frequency discretization arises from the computation and leads to the resolution of the result. Corresponding to each frequency in each time window, a mode number is fitted later on.

For the calculation of mode numbers, it is necessary to gather phase information of the signals. The phase $\varphi_i(\omega)$ follows from equation 4.1. The arcus tangens of the quotient between the imaginary and the real part of the transformed signal $\tilde{S}_i(\omega)$ is taken for each coil, indexed by i.

$$\varphi_i(\omega) = \arctan\left(\frac{\mathrm{Im}(\tilde{S}_i(\omega))}{\mathrm{Re}(\tilde{S}_i(\omega))}\right) \tag{4.1}$$

Due to inductive coupling of the coils to other vessel components, the signals suffer from so-called intrinsic coil phases which alter the measured phase. They are dependent on frequency and differ between coils, which can affect the mode determination. The coils can be modeled as parallel resonant circuits. [27] Measurements on their characteristics result in so called transfer functions $TF_i(f)$. These are meant to correct the signal phases according to equation (4.2).

$$\varphi_i'(f) = \varphi_i(f) + TF_i(f) \tag{4.2}$$

The transfer functions have been measured several times at ASDEX Upgrade, and are tabulated in assorted files. [27] The `mode_determination.py` program reads the right files, corresponding to the chosen discharge number, and incorporates the values to correct the signal phases.

4.1.1 Determination of toroidal mode numbers

From the Fourier transform of each calibrated signal, the phase is calculated. It reads as equation (4.1), which is naturally limited to a co-domain of $\pm\pi$. This information is linked to the position of each coil in terms of toroidal angle. The mode number corresponds to the slope in a signal phase over coil position plot. Since the toroidal mode number is invariant under transformations in ϕ, this process is rather straight forward.

In the simplest case, two coils could attain a mode number, but this would yield no information on the quality of the result. The mode determination program performs a linear regression requiring three or more coils with the residual as a measure for trustworthiness.

The original signal phase gets convoluted into a [-π,π] interval, which means that the phase shift between two coils has an upper bound of 2π. Moreover, ascending phases can appear as descending, and other way round. To compensate, the program divides into a positive and a negative regression loop. Alternating phases in the coil array do not make sense in the physical image of the modes. For the positive loop, each phase with a lower value than the one before it is shifted up by 2π, creating a monotonically ascending array. The exact opposite is done for the negative loop. A linear regression is done in each of the loops and the one with the smallest residual is accepted as the result.

One can see that the detectable mode number is then limited to a phase shift of 2π between the farthest neighboring coils. In the case of the outboard toroidal array, the coils B31-14 and B31-40 are separated by 1.5 rad. This would bring the maximum detectable n to approximately 4.
To enable a larger range, the program offers the option of fit order. A number of shifts is created. For the positive loop, the phase of the last coil in the array is shifted up by 2π and a linear regression is done. The other phases are then shifted one by one and regressions are created likewise. This process is repeated up to a total shift of fit order times 2π in the last coil with every monotonically ascending combination. The respective negative shifts are performed for the negative loop.
For toroidal calculation, sometimes a fit order of 6 is required, which leads to a considerable number of shifts and therefore computing time. In the end, out of all the positive and negative shifts, the one with the smallest residual is taken. Also the residual of that linear fit is saved. Such a fit with according shifts is performed for every frequency step in every time window. [14]

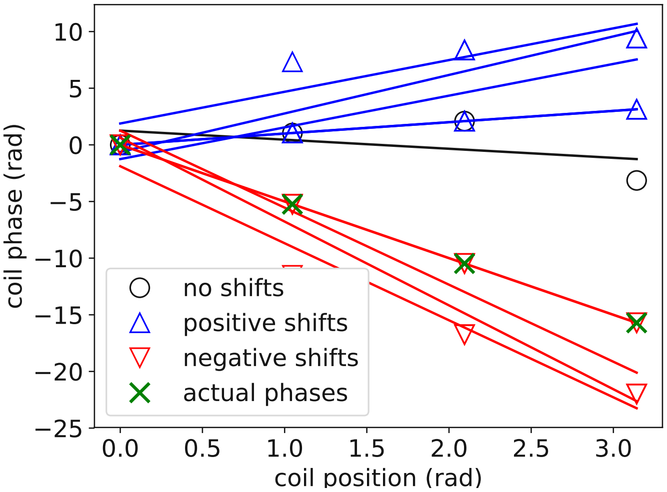

Figure 4.1: Graphical example for the solving of a best mode number fit. The coil position is at the abscissa, the phase is indicated at the ordinate. Green crosses as actual phases, black circles as measured phases, blue triangles as positive shifts and red triangles as negative shifts. Black, blue and red lines show the linear fits. The result with the smallest residual is -5.

Figure 4.1 is a graphical representation of the fitting process. For the sake of clarity, only four coils are included and the fit order equals 1. The coil position is at the abscissa, the phase is indicated at the ordinate. Green crosses indicate where the actual phases lie, black circles represent the measured phases without shifts. The positively shifted phases are blue triangles and the negatively shifted phases are red triangles. Black, blue and red lines indicate the fit through each combination of shifts. The one with the smallest residual is where the green crosses exactly overlay the red triangles and the mode number is correctly identified to be -5. This example is composed of artificial coil positions and phases with no noise added. It is solved by the very algorithm in `mode_determination.py`. At the end of the determination process stands a histogram of intensity over a mode number versus frequency plane. Each fit that comes out at a certain frequency and mode number contributes to the intensity at that position in the histogram. In addition, the inverse of the residual is used to weigh it so worse fits contribute less. The intensity is then normalized to its global maximum. An example plot for the n determination is shown in figure 4.2. The colorbar on the right explains the color coding. Increasing intensity leads from black over red and yellow to white. For the plot, the color coding may be chosen so that features of interest are emphasized. In figure 4.2, there is a bright spot at $n = 1$. This is a structure from inside the plasma, referred to as the core mode, which moves in ion diamagnetic direction and appears in most histograms. It is not subject of this thesis. Other modes can be seen which are arranged in branches and likely lie in the pedestal. Due to their progression in the electron diamagnetic direction, they display negative n.

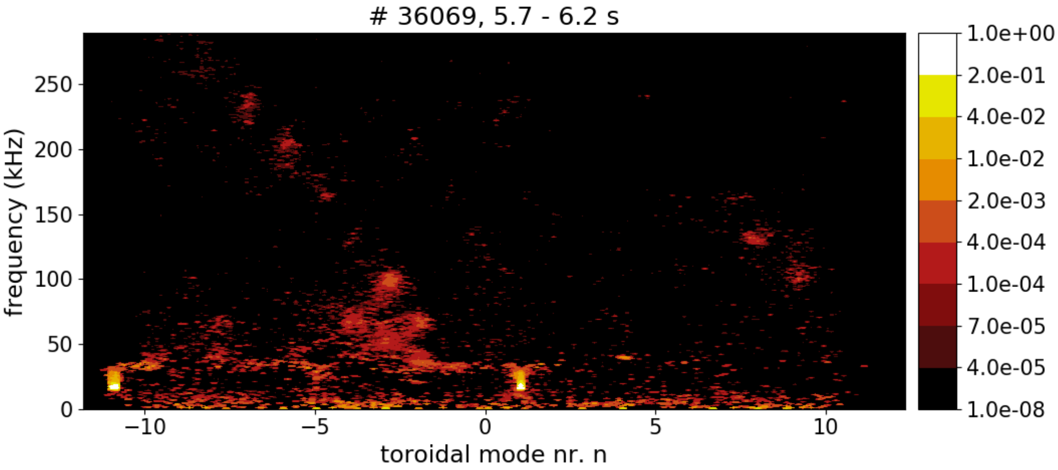

Figure 4.2: Intensity histogram over frequency and mode number n. The colorbar on the right explains the color coding of intensity, increasing from black over red and yellow to white. MHD modes can be seen as intensity maxima in the negative n range.

The intrinsic coil phases are corrected by means of the transfer functions introduced in chapter (4.1). An improving effect of the transfer functions is shown in figure 4.3. The case without transfer functions in figure 4.3a shows a displacement of intensity for some of the modes, which is greatly reduced by including the transfer functions in figure 4.3b.

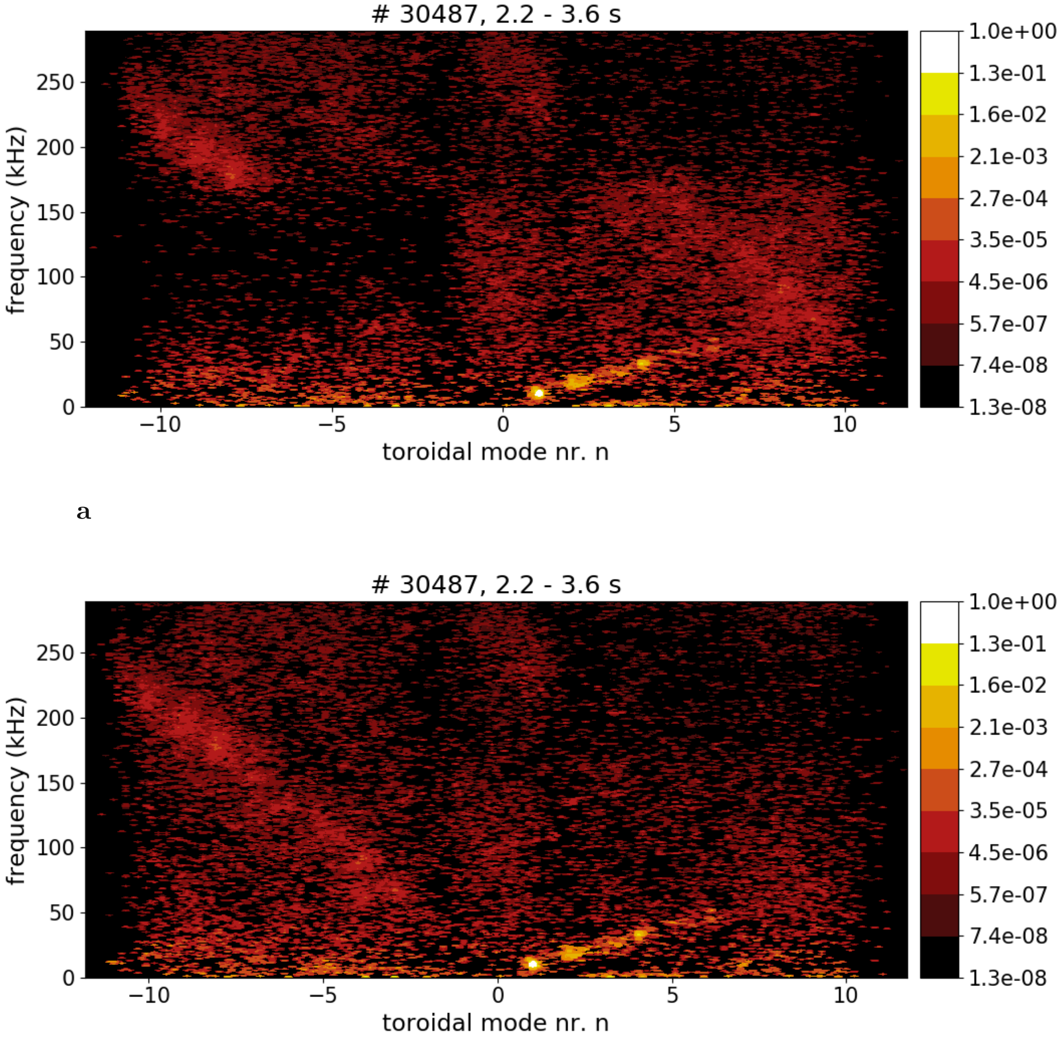

a

b

Figure 4.3: Example for a mode determination result a) without and b) with included transfer functions. Modes are partly displaced in a), but in correct, linear arrangement in b).

4.1.2 Determination of poloidal mode numbers

The determination of poloidal mode numbers m requires additional input and is therefore more intricate. In the usual (θ, ϕ) system, m is not a good quantum number. As the local magnetic field varies along a poloidal revolution, so does the wave vector. The TOKAMAK is symmetrical to toroidal transformations, but not to poloidal ones.

It is for the same reason that the local magnetic field line slope is distinct from the safety factor, a global quantity. To find the true poloidal mode number m, the fitting procedure must be done in a basis where m is a good quantum number. The transformation θ to θ^* is not linear, but bijective and must be numerically extracted from a magnetic equilibrium reconstruction for each locality.

The coils measure the temporal derivative of the radial electric field, so the coil positions are radially projected to flux surfaces. The closer a coil sits to a flux surface, the more accurately the (θ^*, ϕ) coordinates are transferred. Therefore, modes at the plasma edge can be localized more precisely than in the core. Since each coil position is known in the (θ, ϕ) system, the transformation to θ^* can be done. It is founded on the IDE equilibrium reconstruction and calculated using functions from the 2020 `MAP EQ` library by Giovanni Tardini. [34] The poloidal ballooning coil array can then be assigned to straight field line angles. Importantly, field lines and therefore modes lie equidistantly on flux surfaces in the (θ^*, ϕ) frame. This allows to infer the poloidal mode number m as a global quantity from phase shifts between local coils. The whole poloidal ballooning coil array lies relatively tightly packed at the low field side.

As the transformation depends on the radial position in the plasma, a ρ_{pol} locality must be assumed for the calculation. This causes the whole process to be an iterative one, as the correct ρ_{pol} input can only be verified through the mode number result.

The mode numbers m follow from a set of linear regressions of phase over coil position, the process is equivalent to the n determination described in the previous section. The slope of the linear fit with the smallest residual equals the mode number result.

Figure 4.4 displays the result of a poloidal mode number determination. The labels and colorbar are alike figure 4.2.

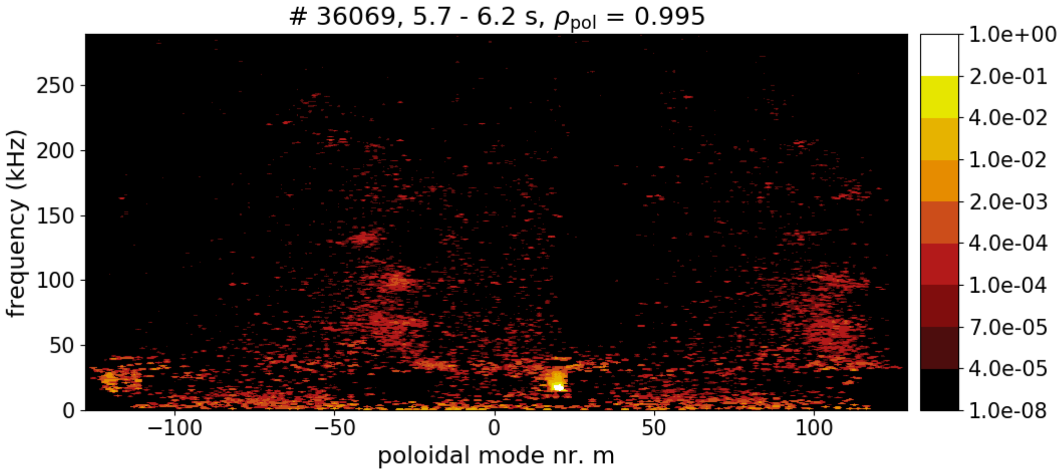

Figure 4.4: Intensity histogram over frequency and mode number m. The colorbar on the right explains the color coding of intensity, increasing from black over red and yellow to white. MHD modes can be seen as intensity maxima in the negative m range.

Increasing the fit order and allowing larger phase shifts can be used to enhance the detection of high m, just as in the n determination. However, the fact that all the coils sit in close proximity to one another, and in nearly equidistant positions, causes small phase shifts in between and allows detection of high m by default. High fit order hardly changes the result of program runs for poloidal mode number determination. An in-depth look into the effect of the coil positions, the fit order and arising errors is taken in the next section.

4.1.3 Artifacts in mode number determination

To interpret mode number histograms like figure 4.2, it is essential to understand what happens when the periodicity of a mode can not be resolved. There are natural limits to the highest and lowest detectable mode numbers. The separation of ballooning coils $\Delta\phi$ sets a resolution, which can be pushed to certain extent with the fit order. If the phase shift between the closest sitting pair of coils exceeds 2π, the measurement becomes ambiguous. This sets the absolute mode number boundary $n_{\max}$, seen in equation 4.3.

$$n_{\max} = \frac{2\pi}{\Delta\phi_{\min}} \tag{4.3}$$

A simulation with coil positions ϕ_i and artificial phases φ_i of known mode number was created to test the limits of the routine. The signals representing a mode number n are at first created like equation 4.4. To mimic the convolution that results from the FFT in measured signals, the phases are then transformed to a $\pm\pi$ co-domain.

$$\varphi_\mathrm{i} = n \cdot \phi_\mathrm{i} \tag{4.4}$$

In practical operation, the routine has to work with phases impaired by noise. This leads to a statistical error in the mode numbers. It is simulated by impinging the artificial phases with a normally distributed random error with an amplitude in the order of 10 % the signal strength. To investigate the statistical effect, the calculation is repeated 100 times for each mode number.
For the determination of the poloidal m, the coil position in the straight field line angle θ^* is used for the calculation. Therefore, the mode number limit is dependent on ρ_pol of the equilibrium, as is θ^*. The calculated coil positions for the equilibrium at $\rho_\mathrm{pol} = 0.98$ of #36069 are listed in table 4.1, those for the outermost equilibrium layer $\rho_\mathrm{pol} = 0.995$ of the same discharge in table 4.2.

coil	θ^*
B31-05	-0.17761
B31-06	-0.12664
B31-07	-0.07680
B31-02	-0.02786
B31-08	+0.02871
B31-09	+0.08083
B31-10	+0.13453

Table 4.1: Positions of coils of the poloidal ballooning array in the straight field line angle, calculated for #36069, $\rho_\mathrm{pol} = 0.98$.

coil	θ^*
B31-05	-0.15010
B31-06	-0.10704
B31-07	-0.06492
B31-02	-0.02356
B31-08	+0.02428
B31-09	+0.06833
B31-10	+0.11371

Table 4.2: Positions of coils of the poloidal ballooning array in the straight field line angle, calculated for #36069, $\rho_\mathrm{pol} = 0.995$.

Figures 4.5 and 4.6 simulate the cases for $\rho_{\mathrm{pol}} = 0.98$ and $\rho_{\mathrm{pol}} = 0.995$, respectively. Green crosses indicate the actual mode numbers, red circles show the determination results for fit order zero and blue diamonds those for fit order 2. The phases represent a branch with mode numbers $-75, -95, -115, -135$ and -155. As can be seen in figure 4.5, the mode numbers down to -115 are recognized correctly with both fit order zero and 2. This can be treated as a minimum performance, as the coils sit closer together for higher ρ_{pol}, which enhances the limit according to equation 4.3. All of the investigated modes are situated in the pedestal, so further outwards than $\rho_{\mathrm{pol}} = 0.98$.

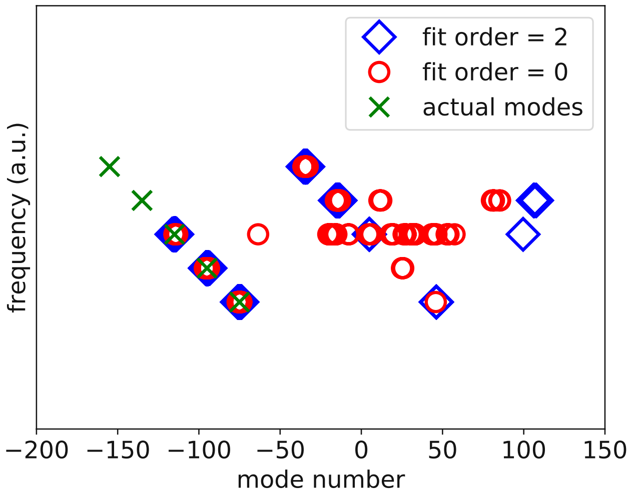

Figure 4.5: Simulated mode number detection for the poloidal ballooning array at #36069, $\rho_{\mathrm{pol}} = 0.98$. The ordinate is a frequency axis in arbitrary units, which is of no importance here. Phases are overlaid with noise to yield a realistic distribution of results. Green crosses indicate the actual mode numbers, red circles show the determination results for fit order zero and blue diamonds for fit order 2. Mode numbers down to -115 are identified correctly. Artifacts congregate in a line parallel to the actual branch.

Figure 4.6 with $\rho_{\mathrm{pol}} = 0.995$ shows a detection limit of -135, again for fit order zero and 2. For the given example, this equals a phase shift of just under $\Delta\varphi = 2\pi$ between neighboring coils.
Other than at the correct positions, results congregate at parallelly shifted positions. This shift amounts approximately the maximum detectable mode number. It is constant, meaning that the linear structure of the branch is reproduced at the shifted position.

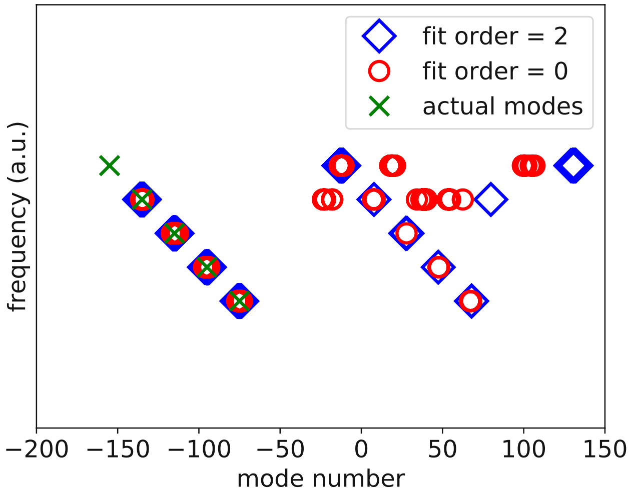

Figure 4.6: Simulated mode number detection for the poloidal ballooning array at #36069, $\rho_{\mathrm{pol}} = 0.995$. The ordinate is a frequency axis in arbitrary units, which is of no importance here. Phases are overlaid with noise to yield a realistic distribution of results. Green crosses indicate the actual mode numbers, red circles show the determination results for fit order zero and blue diamonds for fit order 2. Mode numbers down to -135 are identified correctly. Artifacts congregate in a line parallel to the actual branch.

As can be seen from table 4.1 and 4.2, the poloidal ballooning array is distributed nearly equidistantly, which means that the difference between the limit for fit order zero and the theoretical maximum for infinite fit order, given by equation 4.3, becomes negligible. Thus, increasing of the fit order does not drastically improve the poloidal mode number detection limit.

While the poloidal ballooning array is nearly equidistant, the toroidal ballooning coils are placed irregularly. Table 4.3 holds the fixed toroidal angles of the toroidal ballooning array.

coil	ϕ
B31-40	+2.79148
B31-14	+0.50754
B31-03	-0.53576
B31-01	-1.09941
B31-02	-1.48711
B31-12	-1.53725
B31-13	-2.69327

Table 4.3: Positions of coils of the toroidal ballooning array in the toroidal angle.

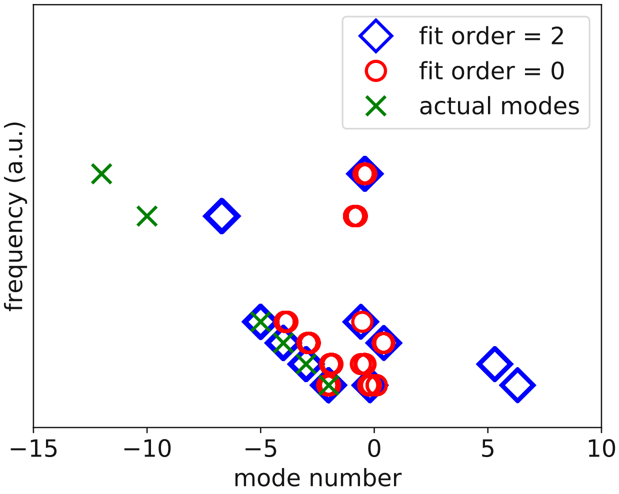

Figure 4.7: Simulated mode number detection for the toroidal ballooning array. The ordinate is a frequency axis in arbitrary units, which is of no importance here. Phases are overlaid with noise to yield a realistic distribution of results. Green crosses indicate the actual mode numbers, red circles show the determination results for fit order zero and blue diamonds for fit order 2. Mode numbers down to -2 are identified correctly with fit order zero, down to -5 is enabled with fit order 2. Artifacts congregate in several locations parallel to the actual branch.

The situation is investigated in figure 4.7. A mode branch including mode numbers $-1, -2, -3, -4, -5, -10$ and -12 is used. The result in figure 4.7 has the same color coding as in figure 4.5. Clearly, the detection for fit order zero is limited to -2, fit order 2 allows down to -5. This is very unsatisfactory as many of the investigated phenomena exceed these mode numbers.
Excluding coil B31-40 increases this limit because that coil is localized farthest from any other. This layout is simulated in figure 4.8. Fit order zero yields correct mode numbers down to -5. However, with a fit order of 2 the $n = -10$ mode can still be recognized, which is typically sufficient. Artifacts copy the linear structure of the branch in parts, but in various locations.

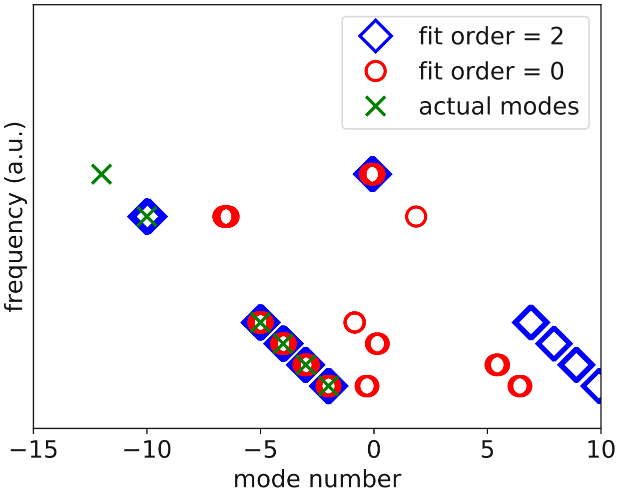

Figure 4.8: Simulated mode number detection for the toroidal ballooning array excluding B31-40. The ordinate is a frequency axis in arbitrary units, which is of no importance here. Phases are overlaid with noise to yield a realistic distribution of results. Green crosses indicate the actual mode numbers, red circles show the determination results for fit order zero and blue diamonds for fit order 2. Mode numbers down to -5 are identified correctly with fit order zero, down to -10 is enabled with fit order 2. Artifacts congregate in several locations parallel to the actual branch.

Irregularly placed coils at fit order zero limit the slope of the fit to 2π between the farthest pair of neighboring coils. Increasing fit order pushes the detectable mode number towards the theoretical limit in equation 4.3, which is governed by the closest sitting coils. Artifacts, meaning wrongly identified modes, appear at mode numbers subjected to a parallel shift. The amount of shift depends on the arrangement of coils. The artifacts might gather at more than one center.

At last, some systematical errors shall be discussed. There could, for instance, be an error in the transfer functions, which would lead to wrong phase information. If the phases in each coil are off by the same margin, the result is of course unaffected. An error that is linearly increasing or decreasing from one coil to the next can explain a parallel up- respectively downshift in the detected mode numbers. The slope of the branch is preserved in this case, only causing a parallel shift. If the error is frequency dependent, the slope of a branch can be affected.

The coil position angles cannot produce a parallel shift for all mode numbers because they are in the denominator of the calculation. However, an error can influence all mode numbers with a constant factor if the coil positions are off by the same factor. This is the case if the equilibrium is evaluated at the wrong position for m determination, for instance.

4.2 Identification of mode branches

Identification of branches stands as the goal of mode number determination. For the naked eye, these linear structures are often apparent. However, bias on the side of the operator or misidentification of structures can lead to errors in the interpretation. The goal of this section is to explain a computational tool that helps to reason mode identification numerically.

In the emergent histograms, modes can be recognized as lightly coloured centers of intensity. Their exact mode numbers and frequencies may be sharply defined, other times their identification is more ambiguous. Figure 4.9 shows a close-up of a well defined mode focal point and falling off intensity to each side. It stems from a toroidal mode number determination of #36069.

In figure 4.10, a close-up of several modes is seen. They belong to the poloidal mode number histogram of discharge #36069. The intensities overlap so that individual positions are indistinguishable. Generally, poloidal mode number histograms seem to produce less clear images of modes. It is often helpful to start with a toroidal mode determination and look for poloidal mode numbers at the resulting frequencies.

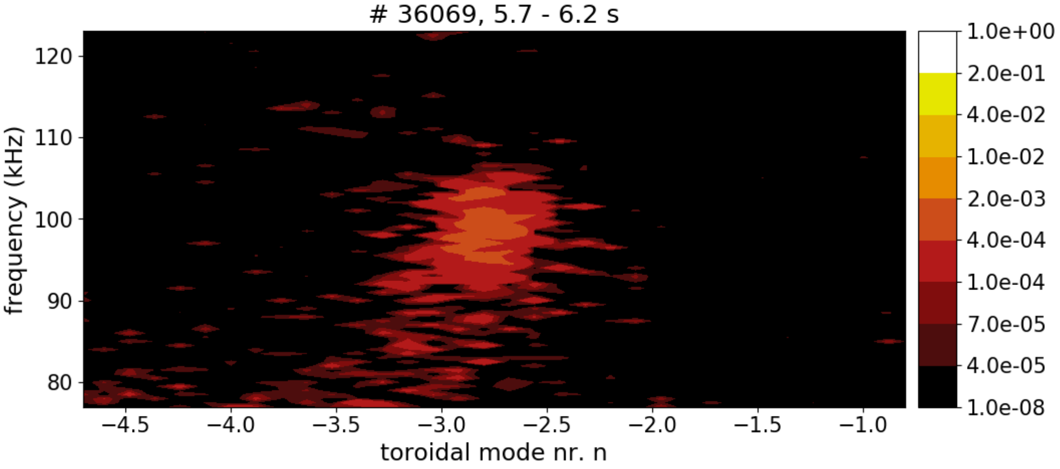

Figure 4.9: Close-up of a well defined mode in a toroidal mode number histogram. A focal point with high intensity, as well as a surrounding area with falling off intensity, are clearly visible.

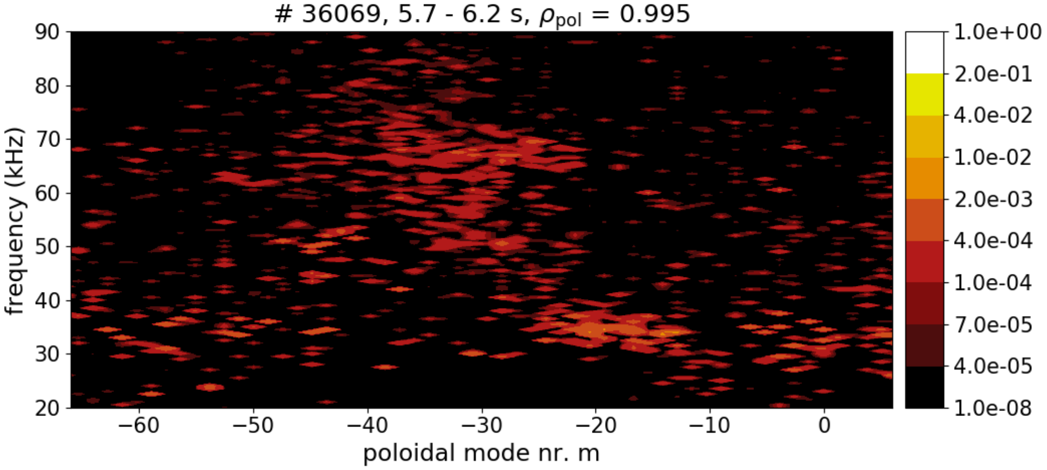

Figure 4.10: Close-up of an area with several modes in a poloidal mode number histogram. The intensities of the modes somewhat overlap and make individual positions indistinguishable.

A routine was devised to recognize modes in histograms with auxiliary input from the operator. It sports different functions.

The first function applies a least square fit of a normal distribution to find the precise focal point of a mode. As the intensity falls off all around, this is an eligible distribution. The function requires initial parameters as input, which include mode number and frequency, respective width and amplitude. This, of course, means influence from the operator. Anyway, the fit will only converge to peaks and is therefore stable against false positives. The validity of results can be assessed from the width and the amplitude after optimization. If the width is disproportional to the width of the mode or the amplitude vastly differs from the maximum intensity of considered mode, the fit cannot be trusted. For clear modes like in figure 4.9, the function yields promising results. Cross checks with areas lacking visible modes show that the fit mostly ends at the maximum iteration number and raises `RuntimeError`.

For the case that a mode is too distorted for the fit to converge, there is the alternative to calculate its center of intensity. This is done by a second function, which also takes initial inputs. The calculation takes a rectangular area in account, which is specified by the operator through the center and size. The function then calculates the center of intensity within this area. Unlike for the fit, a small change of the initial parameters will always affect the result. This method is hence more prone to bias. On the upside, the calculation of the center will always yield a result and can be the right choice for distorted modes. Furthermore, there is also the option of directly entering the coordinates to a mode, which then entirely relies on the operators assessment.

Once at least three modes are added in one of the described ways, a linear regression can be fitted. This yields a slope which is necessary for the localization and velocity calculation of a branch. An additional parameter is the offset, expressed as frequency at mode number zero, as not every branch seems to cross the coordinate origin. A standard error for the slope is also returned, but not for the offset. The uncertainties of the slopes given in the next chapter are based on this.

Which modes form a branch together is, again, evaluated by the operator. A comparison of related poloidal and toroidal mode number histograms is often helpful in deciding this. More than one branch can be defined which allows comparison between differently moving modes.

For #36069, a number of identified modes together and two branches are indicated in the poloidal and toroidal mode number histogram, shown in figure 4.11 and 4.12, in that order. Branches and the modes belonging to them are then highlighted in bright green.

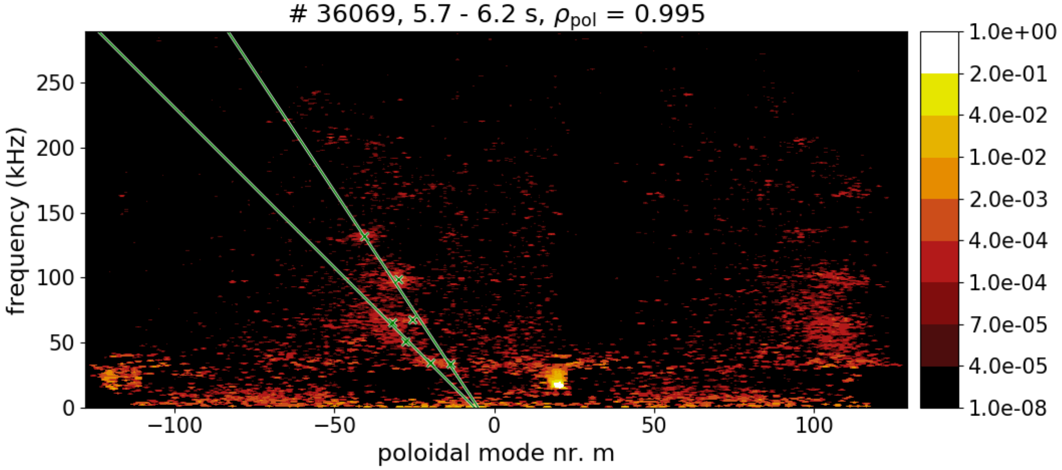

Figure 4.11: Poloidal mode number histogram of #36069 with several modes indicated as green crosses and two branches fitted through as green lines.

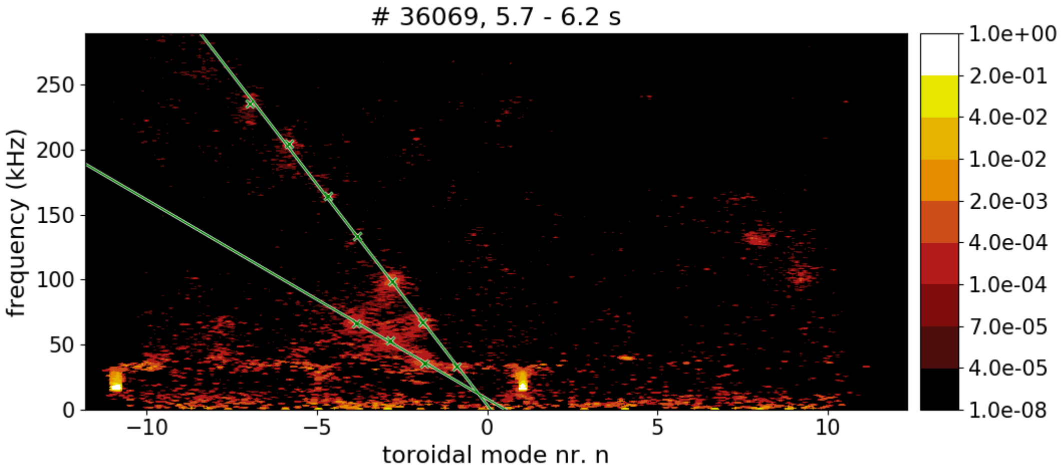

Figure 4.12: Toroidal mode number histogram of #36069 with several modes indicated as green crosses and two branches fitted through as green lines.

To compare the various drift velocities to mode frequencies, a mode velocity projected to the perpendicular field direction must be calculated. The formula used is equation 4.5, where f/n is the branch slope, $B_{\mathrm{pol}}/|B|$ the fraction of poloidal component to absolute magnetic field and $2\pi R$ the torus circumference on the outboard midplane. Uncertainties in f/n are linearly transferred to the mode velocity.

$$v_{\mathrm{mode}} = \frac{f}{n} \cdot \frac{B_{\mathrm{pol}}}{|B|} \cdot 2\pi R \tag{4.5}$$

The frequency of a mode measured at a fixed position suffers from the so-called barber pole effect. This can be thought of as a helical line drawn around a pole. When the pole rotates, the line seems to move along the axis of the pole. Modes sitting at magnetic field lines underlie the same phenomenon, where direction of movement is toroidal. However, this is no physical velocity. To yield a perpendicular velocity without this contribution, the factor $B_{\mathrm{pol}}/|B|$ is multiplied. [35]

The safety factor used for localization is the quotient of toroidal and poloidal branch slopes f/n and f/m, equation 4.6.

$$\frac{f}{n} : \frac{f}{m} = \frac{m}{n} \tag{4.6}$$

Uncertainties given for m/n follow from error propagation of the slopes.

4.3 Drift velocities

To find the ion diamagnetic and electron diamagnetic velocities according to equation 2.16, density and temperature profiles are needed. The density n is measured by the Thomson scattering diagnostic, together with the electron temperature T_{e}. The ion temperature T_{i} on the other hand can be taken from the CXRS diagnostic. The data come as points resolved in space and time. As the analysis is focused on the pre-ELM phase, the data must be temporally filtered in the sense of ELM synchronization. In the presented cases, the ELM window for the profiles stretches from −5.5 ms to the ELM onset. The window is longer compared to the mode determination to gather more data from the profiles, which reduces statistical errors later in the process.

As the gradient is needed in equation 2.16, suitable coordinates must be found to calculate it. On the midplane, the gradient in curved coordinates can be simplified to just the partial derivative in R. Ideally, the data should be given over the radius R on the midplane. Thomson scattering uses a vertically directed laser, so the acquisition points sit at a fixed radius in different z-positions. Like other quantities, density and temperature are assumed to be constant on a flux surface. With the help of a flux coordinate, it is possible to map data points to the midplane. The program `fusionfit` by Philip A. Schneider aids this process. All transformations between cylindrical and flux coordinates depend on an equilibrium reconstruction. Thomson scattering acquisition points are being linked to ρ_{pol} values. The entire profiles are then shifted to match the position of $T_{\mathrm{e}} = 100\,\mathrm{keV}$ with the separatrix at $\rho_{\mathrm{pol}} = 1$ according to the two-point model. [30]

Following this, all profiles are mapped to R so the gradient can be calculated in SI units. The data acquisition of CXRS is already resolved in the radius R and does not need correction with respect to the separatrix.

The raw data over radius are approximated with a spline function. Each data point from the diagnostics comes with an error estimate which acts as a weight for the spline. In addition to the spline function itself, the confidence of the result is of interest. The errors of individual data are already included in the calculation as weights for the spline. Instead, the confidence of the spline is determined via a sampling algorithm using the covariance of the spline parameters. Normally distributed vectors are created 100 times and multiplied to the matrix square root of the covariance matrix. The resulting vectors are added to the parameter vector to create a set of normally distributed parameter vectors for the spline. From this set, a standard deviation can be calculated. The credit for this method goes to Dirk Nille.

Splines are advantageous because they can be differentiated easily. With the method explained above, it is also easy to translate errors to the derivative of a function. Hence profiles and gradients of temperature and density are available as analytical functions. The relevant pressure gradient can then be easily calculated as equation 4.7.

$$\nabla p = k_\mathrm{B}(\nabla n \cdot T + n \cdot \nabla T) \tag{4.7}$$

An example for the electron density of #36327 is given in figure 4.13, with data points as red dots and the spline function as a blue line. The very narrow confidence interval is indicated by green, dashed lines.

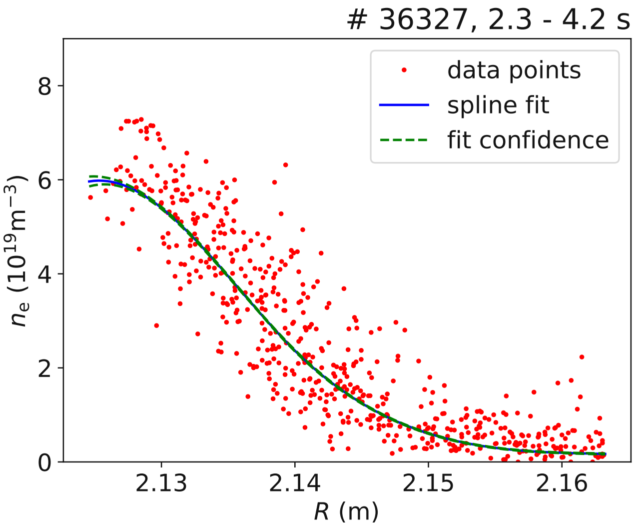

Figure 4.13: Data points in red, spline fit in blue and fit confidence in green for the electron density profile of #36327.

Finished velocity profiles for #36327 can be seen in figure 4.14. The ion diamagnetic velocity fit appears as a red line, with the confidence interval as rose, dashed lines. The electron diamagnetic velocity is shown as a blue line, with the confidence interval as cyan, dashed lines.

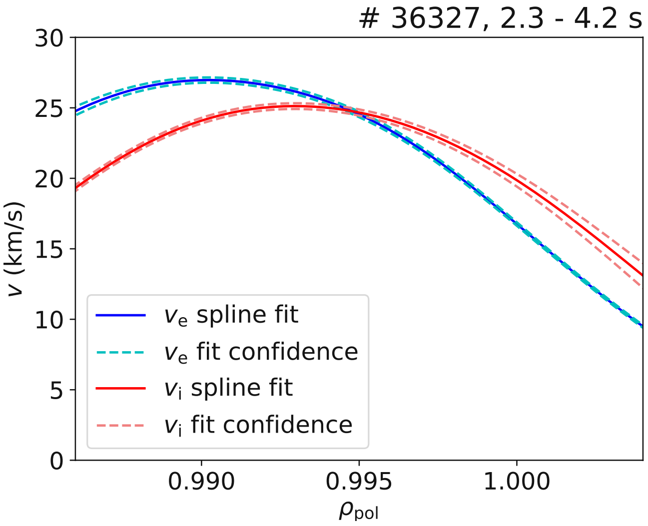

Figure 4.14: Fitted profiles of ion diamagnetic velocity in red, with confidence interval in rose as well as electron diamagnetic velocity in blue and confidence interval in cyan, all from #36327.

Chapter 5

Localization

Applying the methods presented in the previous chapter, data from several discharges are investigated. Each discharge is discussed with respect to its plasma parameters and operational regime. The histograms are then analyzed for their relevant features. Especially, the slope of mode branches is determined. With help of IDE equilibrium reconstructions, an attempt is made to localize the modes.

5.1 #33211

This first discharge was chosen for its clear display of modes, even though edge profiles and velocities are missing. It is described as evolution of the pedestal in the inter-ELM phase with varying triangularity. The toroidal magnetic field is nearly $-2.5\,\mathrm{T}$, the plasma current is about $0.8\,\mathrm{MA}$. The plasma is heated by neutral beam injection and electron cyclotron resonance heating. Table 5.1 holds the parameters that characterize the plasma. A time interval from $2.5\,\mathrm{s}$ to $3\,\mathrm{s}$ is selected, in which heating power and radiation are stable.

B_{tor}	$-2.487\,\mathrm{T}$
I_{plasma}	$0.800\,\mathrm{MA}$
q_{95}	5.052
P_{ECRH}	$1.423\,\mathrm{MW}$
P_{NBI}	$5.019\,\mathrm{MW}$

Table 5.1: Parameters of #33211.

Figure 5.1 shows the toroidal mode number histogram of discharge #33211. It displays a very clear branch of eight modes spanning through the negative n range. The core mode sits at $n = 2$ here. The modes at $n = -4$ and $n = -5$ produce artifacts on the right. Upon close inspection, the modes $n = -1$, $n = -6$ and $n = -7$ appear split as if possessing two separate maxima. Fitting with a normal distribution suggests that they are in fact separate modes.

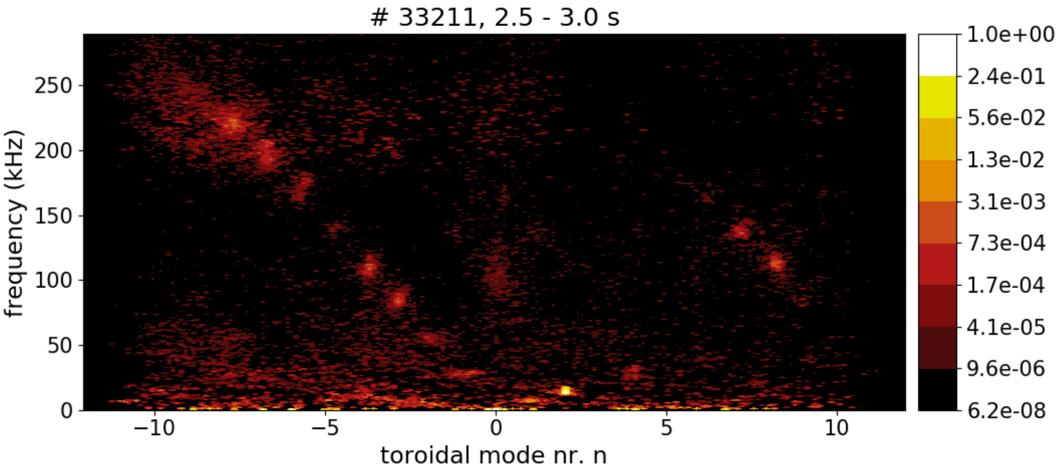

Figure 5.1: Toroidal mode number histogram of #33211. Modes down to $n = -8$ appear in the left half of the image. On the right, the modes $n = -4$ and $n = -5$ produce artifacts.

Figure 5.2 shows the fitted positions of eight aligned modes in #33211 as green crosses. The branch assembled by these modes is indicated by a green line and has a slope of $-29.27 \pm 0.50\,\mathrm{kHz}$ and an offset of $-1.87\,\mathrm{kHz}$.

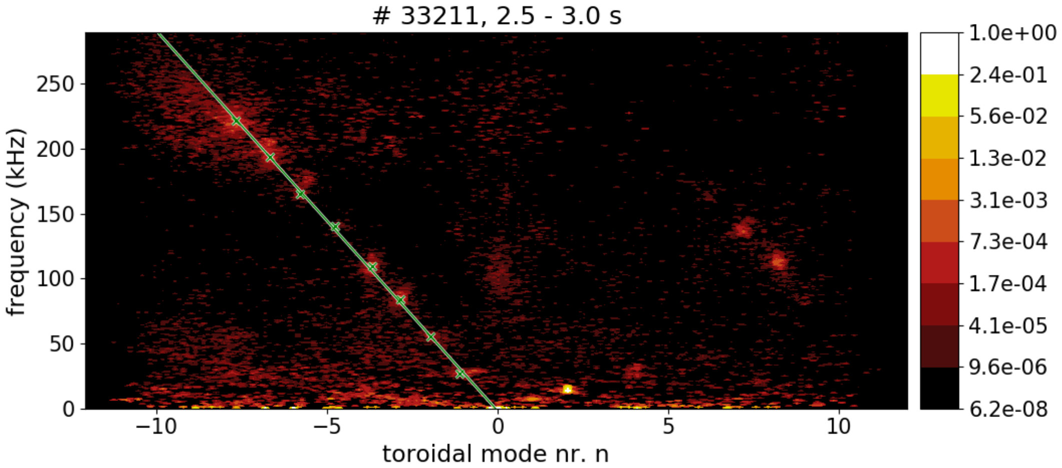

Figure 5.2: Toroidal mode number histogram of #33211. The mode branch is identified with green crosses and a green line.

From the double maxima, which lie off the first branch, another branch can be constructed. This is shown in figure 5.3, resulting is a slope of $-29.29 \pm 0.56\,\mathrm{kHz}$ and an offset of $10.25\,\mathrm{kHz}$, almost parallel to the first branch. Table 5.2 gives the fitting results of all the modes.

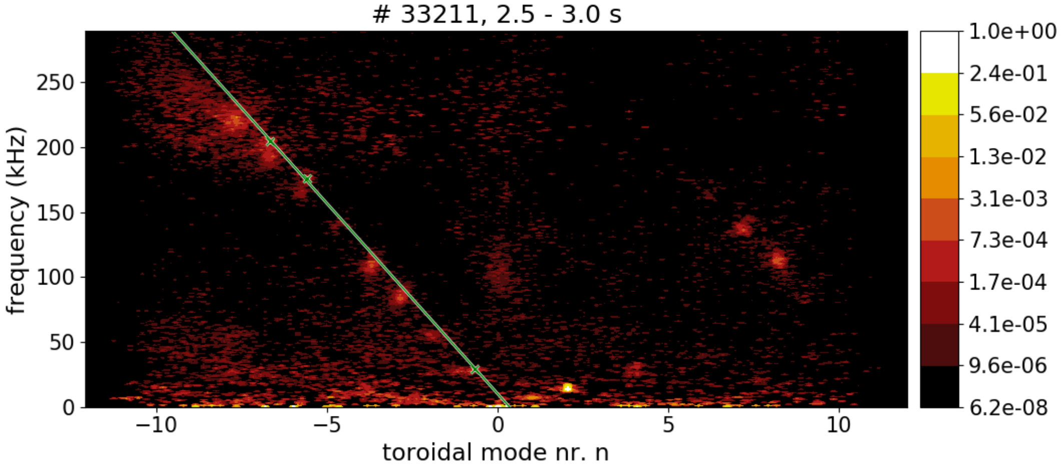

Figure 5.3: Toroidal mode number histogram of #33211. An alternative branch through the outlying modes is identified with green crosses and a green line.

mode	n	f (kHz)
branch 1		
1	-1.13	27.0
2	-1.96	55.3
3	-2.85	83.8
4	-3.69	109.9
5	-4.76	140.3
6	-5.79	165.0
7	-6.69	193.8
8	-7.69	221.5
branch 2		
1	-0.66	29.3
2	-5.59	175.8
3	-6.69	204.7

Table 5.2: Modes in the n histogram of #33211 with mode numbers and frequencies.

Continuing with the poloidal mode numbers, figure 5.4 shows a histogram of #33211 with the equilibrium evaluated at $\rho_{\text{pol}} = 0.98$, in the pedestal. A core mode is visible in bright yellow at about $m = 15$. As the poloidal mode number is evaluated in the pedestal region, this is not the correct m of the core mode. In the negative m range, there are five modes arranged in a branch, the fifth of which is very faint. The branch reaches to closely under 150 kHz. On the positive m side, two artifacts appear, which correspond to the two topmost modes of aforementioned branch. Above their frequency, there is some intensity which could be vaguely identified as three modes. Due to the position, it is likely that this is also an artifact belonging to negative m. However, it does not seem to align with the branch, being shifted but nearly parallel to it.

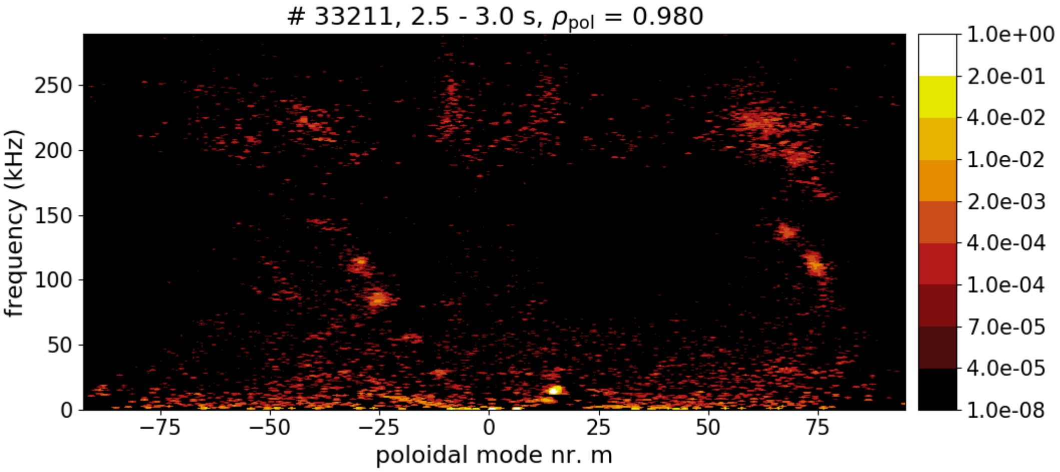

Figure 5.4: Poloidal mode number histogram of #33211 applying $\rho_{\text{pol}} = 0.98$. A branch of five modes slopes in the left half of the image. On the right, artifacts are visible.

The five modes and the branch they form are marked in figure 5.5 with green crosses and a green line. All mode numbers and frequencies are given in table 5.3. The branch results in a slope of $-4.44 \pm 0.29\,\mathrm{kHz}$ and an offset of $-23.48\,\mathrm{kHz}$.

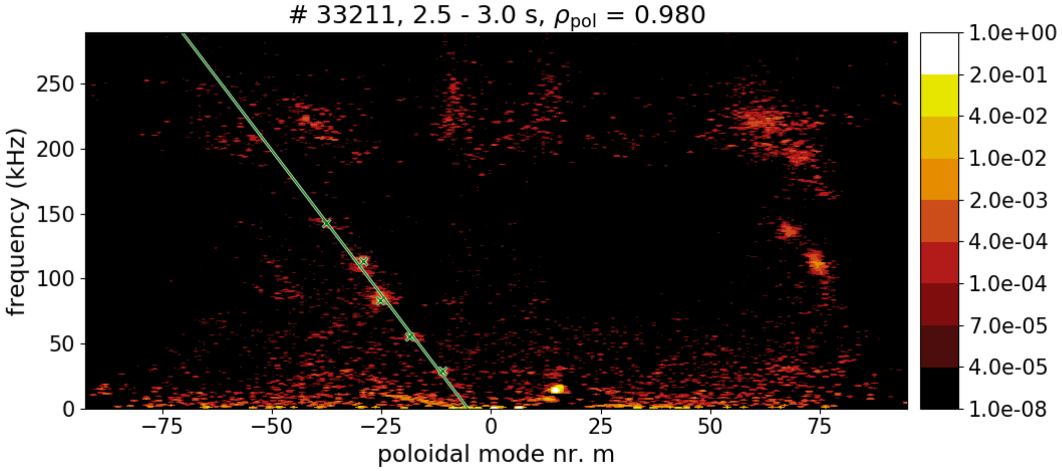

Figure 5.5: Poloidal mode number histogram of #33211 with $\rho_{\mathrm{pol}} = 0.98$. The mode branch is identified with green crosses and a green line.

mode	m	f (kHz)
1	-11.19	28.9
2	-18.65	55.7
3	-25.26	83.6
4	-29.15	113.6
5	-37.67	142.6

Table 5.3: Modes in the m histogram of #33211 and $\rho_{\mathrm{pol}} = 0.98$ with mode numbers and frequencies.

From the quotient of the slopes, the safety factor can be estimated. However, one problem is that especially the branch in m shows a significant offset. Based on the artifacts described in chapter 4.1.3, an artificial offset could occur while the slope is correctly preserved. Another argument for an offset are the wave phenomena discussed in chapter 2.4. When neglecting the offsets and assuming correct slopes, the safety factor follows from figure 5.2 and 5.5 to $q = 6.58 \pm 0.45$.

Based on the equilibrium reconstruction IDE, q equals 4.85 at $\rho_{\mathrm{pol}} = 0.98$, so clearly below the estimate based on the mode numbers. As mentioned before, the localization process is an iterative one with changes to the ρ_{pol} input.
Figure 5.6 shows another poloidal mode number histogram of #33211. The equilibrium is evaluated at $\rho_{\mathrm{pol}} = 0.995$, the outermost position available. As can be seen, this increases the mode numbers while maintaining the general structure compared to $\rho_{\mathrm{pol}} = 0.98$. Green crosses indicate the modes, the branch is shown as a green line. The result is a slope of $-3.74 \pm 0.25\,\mathrm{kHz}$ and an offset of $-23.53\,\mathrm{kHz}$. The modes are listed in table 5.4.

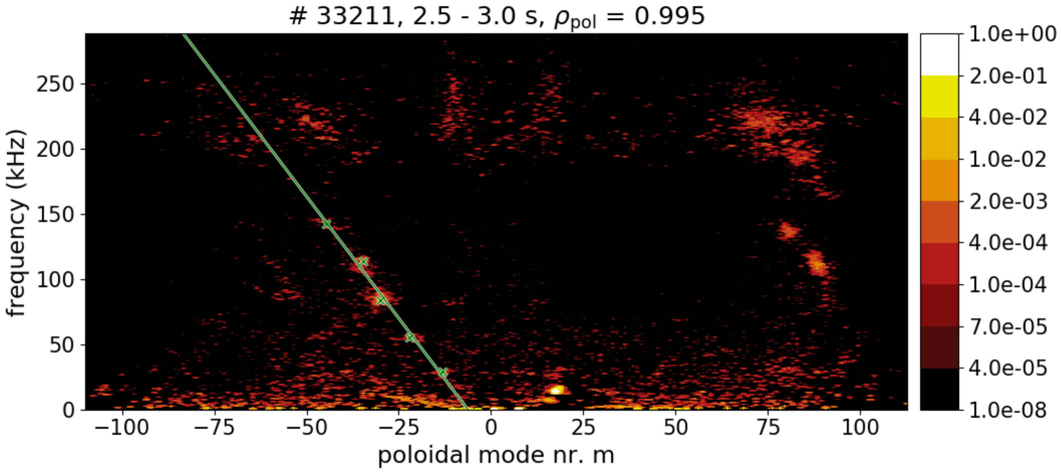

Figure 5.6: Poloidal mode number histogram of #33211 with $\rho_{\mathrm{pol}} = 0.995$. The mode branch is identified with green crosses and a green line.

mode	m	f (kHz)
1	-13.30	28.9
2	-22.15	55.7
3	-30.00	83.6
4	-34.62	113.6
5	-44.74	142.6

Table 5.4: Modes in the m histogram of #33211, $\rho_{\mathrm{pol}} = 0.995$ with mode numbers and frequencies.

To examine the safety factor further inside of the plasma, yet another poloidal mode number determination is performed at $\rho_{\text{pol}} = 0.94$. The result can be seen in figure 5.7. The structure of the histogram is preserved compared to the previous cases in figure 5.5 and 5.6, as the mode numbers are only changed by a multiplicative factor. Green crosses indicate the modes, a green line depicts the branch with a slope of -5.41 ± 0.36 kHz and an offset of -23.83 kHz. Table 5.5 holds the individual modes.

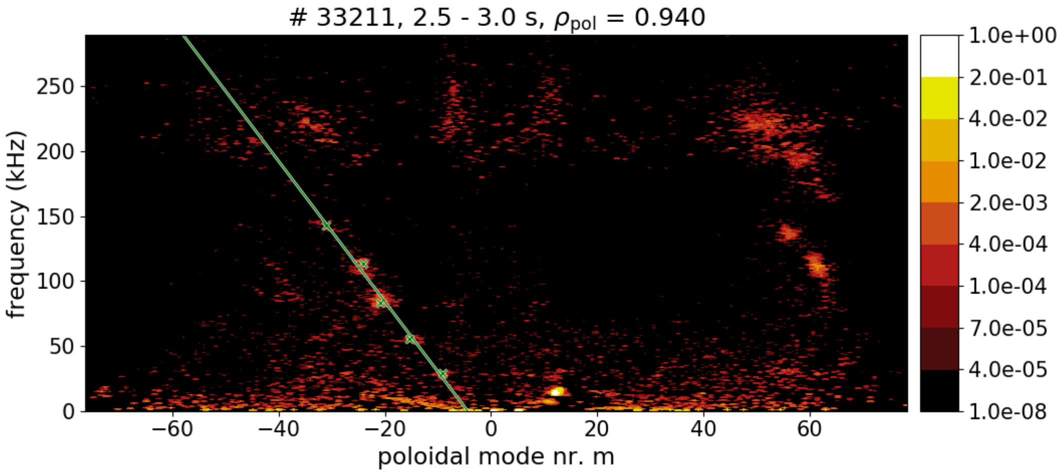

Figure 5.7: Poloidal mode number histogram of #33211 with $\rho_{\text{pol}} = 0.94$. The mode branch is identified with green crosses and a green line.

mode	m	f (kHz)
1	-9.24	28.9
2	-15.39	55.7
3	-20.85	83.6
4	-24.06	113.6
5	-31.04	142.6

Table 5.5: Modes in the m histogram of #33211, $\rho_{\text{pol}} = 0.94$ with mode numbers and frequencies.

Figure 5.8 shows the q profile based on IDE as green triangles, next to m/n as purple circles with error bars, based on the branch slopes for each position. Table 5.6 holds the corresponding numbers. The m/n values lie above the q profile, while the relative difference shrinks slightly towards the separatrix. It could be concluded that both values converge outside of $\rho_{\mathrm{pol}} = 0.995$, which would be the locality of the modes.

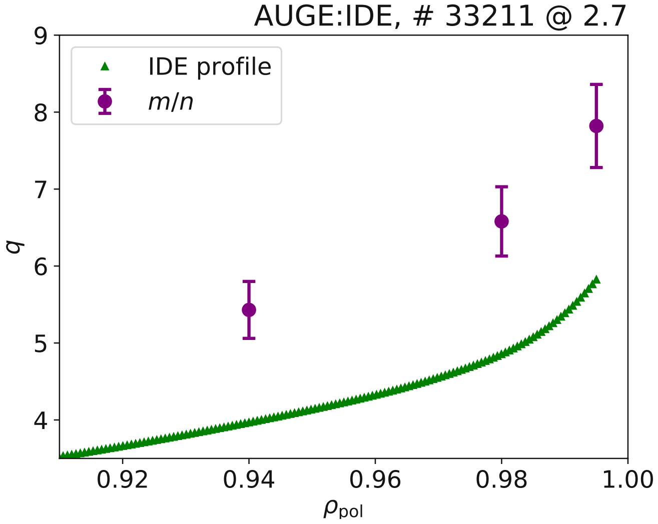

Figure 5.8: Safety factor over flux coordinate for #33211. The green triangles indicate the profile from IDE, the purple circles with error bars show the m/n values found.

ρ_{pol}	m/n	q
0.94	5.41 ± 0.37	3.97
0.98	6.58 ± 0.45	4.85
0.995	7.82 ± 0.54	5.82

Table 5.6: Values of q from IDE, along with m/n at each position for #33211.

5.2 #36068

This discharge is focused on the type-I ELM regime in a plasma with high triangularity. It shows a mode structure in the pedestal and unlike in #33211, drift velocity profiles are available. Table 5.7 gives the operational parameters. The following analysis is based on the interval from 4.8 s to 5.3 s in the discharge.

B_{tor}	$-2.502\,\mathrm{T}$
I_{plasma}	$1.056\,\mathrm{MA}$
q_{95}	4.189
P_{ICRH}	$3.725\,\mathrm{MW}$
P_{NBI}	$5.009\,\mathrm{MW}$

Table 5.7: Parameters of #36068.

To begin with, the toroidal mode numbers of #36068 can be seen in figure 5.9. There is a core mode at $n = 1$ and a fairly visible branch stretching with negative slope from $n = -1$ to -9. Artifacts in the right half of the image between 100 and 150 kHz are likely produced by the modes $n = -4$ and -5. Any remaining intensity cannot be assigned to any specific structure.

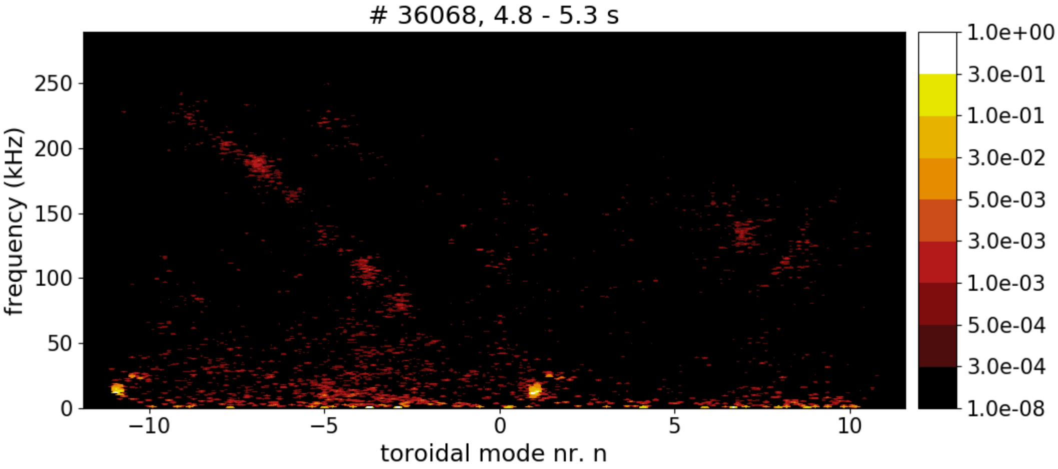

Figure 5.9: Toroidal mode number histogram of #36068. A core mode at $n = 1$ and a branch from $n = -1$ to -9 are visible.

The mentioned branch is fully identified and fitted in figure 5.10. The branch has a slope of $-25.88 \pm 0.64\,\mathrm{kHz}$ and an offset of $4.50\,\mathrm{kHz}$. All detected modes are listed in table 5.8.

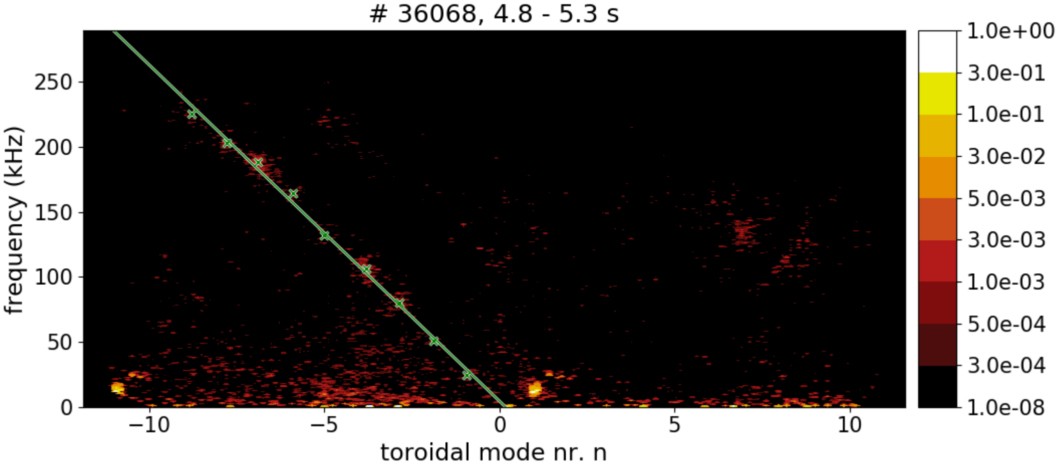

Figure 5.10: Toroidal mode number histogram of #36068. The mode branch is identified with green crosses and a green line.

mode	m	f (kHz)
1	-0.94	24.8
2	-1.87	50.9
3	-2.87	80.0
4	-3.81	106.3
5	-4.99	132.3
6	-5.90	164.2
7	-6.89	188.7
8	-7.79	202.9
9	-8.79	225.5

Table 5.8: Modes in the n histogram of #36068 with mode numbers and frequencies.

The respective poloidal mode numbers are shown in figure 5.11. An equilibrium reconstruction at $\rho_{\mathrm{pol}} = 0.995$ is applied. Apart from the core mode, the structures are much less clear than in figure 5.9. Two modes between 100 and 150 kHz are most apparent. A rather faint one aligned with them lies below. There is another visible mode around 200 kHz, but not aligned with the others.

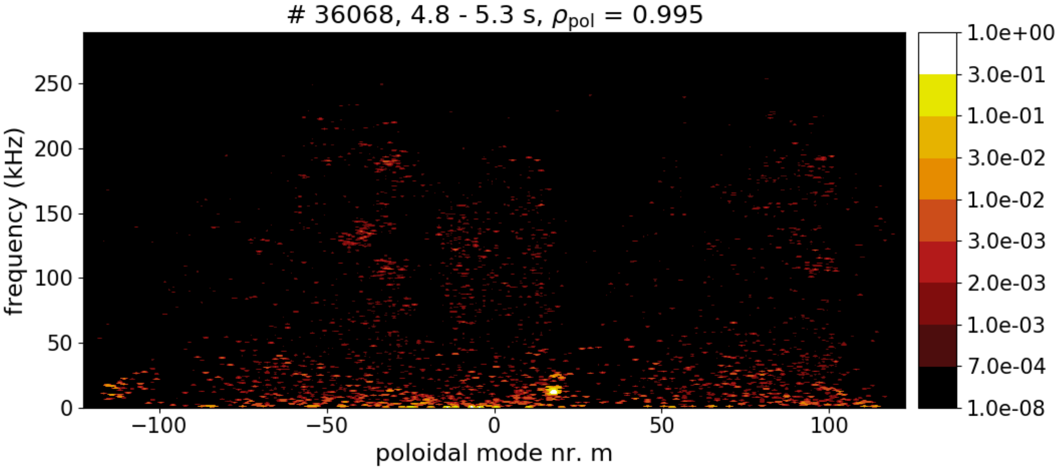

Figure 5.11: Poloidal mode number histogram of #36068 with $\rho_{\mathrm{pol}} = 0.995$. A core mode and individual modes in the negative m range from 100 to 200 kHz are visible.

Figure 5.12 shows the corresponding fit. Three aligned modes could be detected and form a branch with a slope of $-3.97 \pm 0.52\,\mathrm{kHz}$ and an offset of $-23.58\,\mathrm{kHz}$. The mode numbers and frequencies are held in table 5.9.

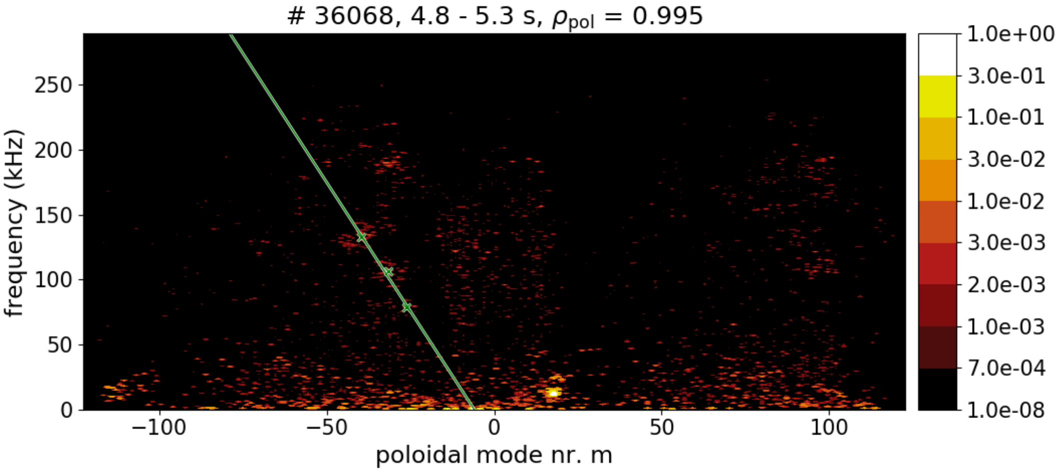

Figure 5.12: Poloidal mode number histogram of #36068 with $\rho_{\mathrm{pol}} = 0.995$. The mode branch is identified with green crosses and a green line.

mode	m	f (kHz)
1	-26.38	78.7
2	-31.70	106.3
3	-39.84	133.0

Table 5.9: Modes in the m histogram of #36068, $\rho_{\mathrm{pol}} = 0.995$ with mode numbers and frequencies.

The poloidal mode number determination for $\rho_{\text{pol}} = 0.94$ and 0.98 is performed as well, which differs from $\rho_{\text{pol}} = 0.995$ only by a factor again. Only the results for m/n of the branches are presented here, as well as for the following discharges. Figure 5.13 displays them as purple circles with error bars, along with the respective q profile of #36068 as green triangles. The values are listed in table 5.10. For each equilibrium position, m/n is greater than q. In this case, the modes seem to be localized outside of $\rho_{\text{pol}} = 0.995$ as well.

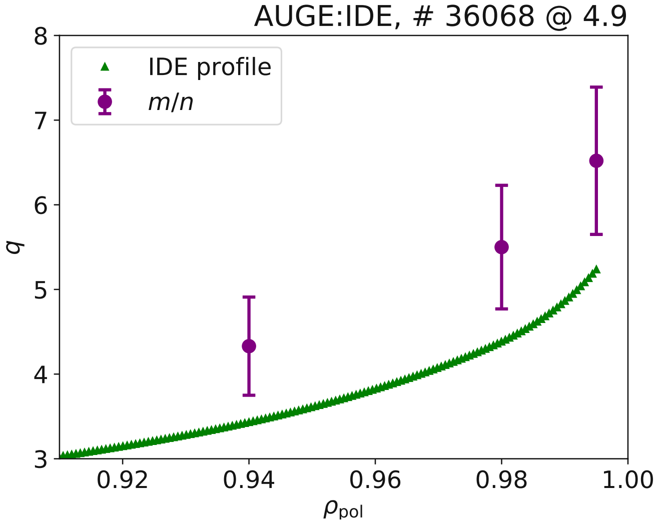

Figure 5.13: Safety factor over flux coordinate for #36068. The green triangles indicate the profile from IDE, the purple circles with error bars show the m/n values found.

ρ_{pol}	m/n	q
0.94	4.33 ± 0.58	3.43
0.98	5.50 ± 0.73	4.38
0.995	6.52 ± 0.87	5.24

Table 5.10: Values of q from IDE, along with m/n at each position for #36068.

Thanks to sufficient CXRS data, velocity profiles are available for #36068. Figure 5.14 compares the v_{ExB} data from EER and the electron diamagnetic velocity based on chapter 4.3 to the velocity of the modes, projected perpendicularly to the magnetic field. Green circles with error bars depict v_{ExB}, the blue line with cyan uncertainty shows the electron diamagnetic velocity and the purple line with violet uncertainty is the mode velocity. Based on where the modes are localized, R and $\vec{B}$ as used in equation 4.5 change and give rise to the purple curve. As can be easily judged, the mode velocity vastly exceeds the combined electric field and electron diamagnetic drift, so an additional effect must be involved.

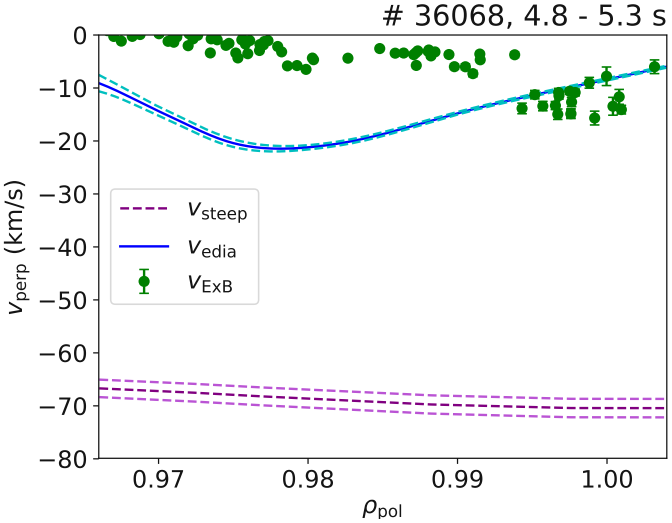

Figure 5.14: Comparison of velocity profiles over flux coordinate for #36068. Green circles with error bars depict v_{ExB}, the blue line with cyan uncertainty shows the electron diamagnetic velocity and the purple line with violet uncertainty is the mode velocity.

5.3 #36069

In many respects, this discharge is similar to #36068 as it also lies in the regime of high triangularity type-I ELMs. The heating power with ICRH is slightly higher while the plasma current is lower compared to #36068. A difference can be seen in the increased q_{95}. The parameters can be seen in table 5.11. As a time interval, 5.7 s to 6.2 s is chosen.

B_{tor}	$-2.502\,\mathrm{T}$
I_{plasma}	$0.797\,\mathrm{MA}$
q_{95}	5.415
P_{ICRH}	$3.749\,\mathrm{MW}$
P_{NBI}	$5.061\,\mathrm{MW}$

Table 5.11: Parameters of #36069.

In figure 5.15, the histogram of toroidal mode numbers for #36069 can be seen. Its core mode appears at $n = 1$. Most prominently, there are two clearly separated branches in this discharge, both with negative n. The steeper one reaches from $n = -1$ to -7. Diffuse intensity corresponding to $n = -8$ is to faint for clear identification. On the right, artifacts arise from the modes $n = -3$, -4 and to a lesser degree $n = -5$. The flatter branch includes the mode numbers -2,-3 and -4. As both branches converge near the coordinate origin, $n = -1$ of the steep branch and $n = -2$ of the flat branch are hard to distinguish.

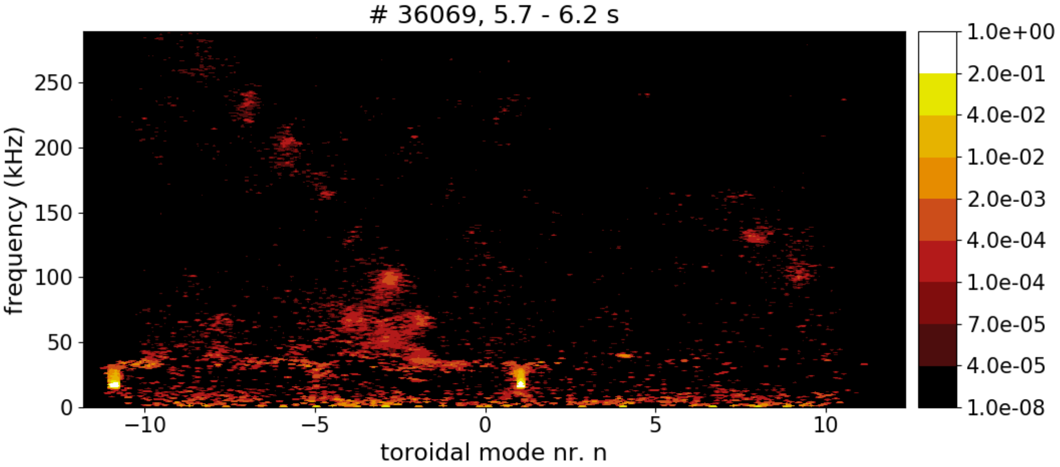

Figure 5.15: Toroidal mode number histogram of #36069. The core mode is at $n = 1$. Two branches of different slope are apparent in the negative n range. On the right, artifacts of $n = -3$ to -5 are visible.

Figure 5.16 highlights these features. The modes are listed in table 5.12. For the steep branch, the fit yields a slope of −34.01 ± 0.53 kHz and an offset of 3.36 kHz. The flat branch results in a slope of −15.33 ± 1.61 kHz and an offset of 8.10 kHz.

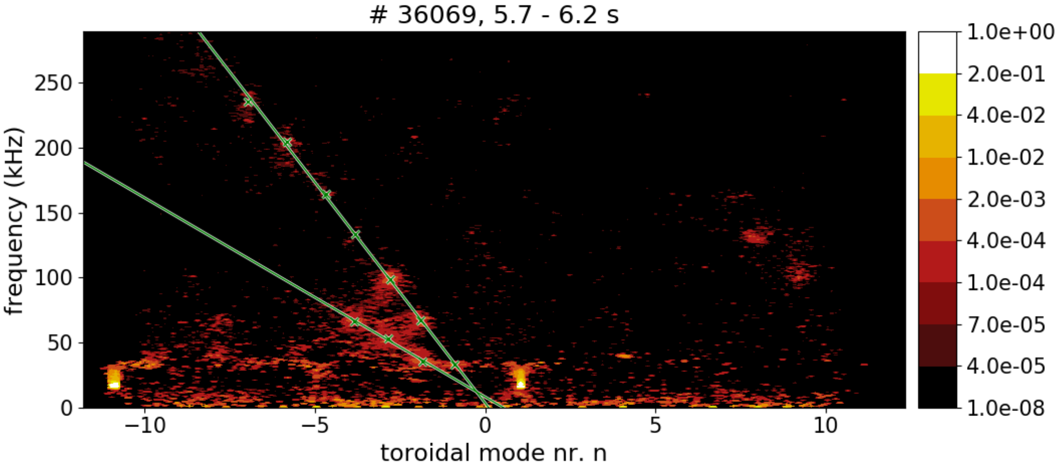

Figure 5.16: Toroidal mode number histogram of #36069. The modes and branches are identified with green crosses and green lines.

mode	n	f (kHz)
branch 1		
1	-0.90	33.1
2	-1.91	66.7
3	-2.79	98.9
4	-3.82	133.4
5	-4.66	164.4
6	-5.81	204.4
7	-6.96	235.9
branch 2		
1	-1.86	35.7
2	-2.84	53.5
3	-3.86	66.4

Table 5.12: Modes in the n histogram of #36069 with mode numbers and frequencies.

The poloidal mode number histogram of #36069 with $\rho_{\mathrm{pol}} = 0.995$ can be seen in figure 5.17. The core mode mistakenly appears around $m = 20$, being evaluated at the very edge. Both branches are much less recognizable. Four modes of the steep branch show under 150 kHz. The flat branch hardly shows any discernible modes, but intensity is seen below the steep branch. Its frequency range is consistent with the flat branch from figures 5.15 to 5.16. At roughly 30 kHz between $m = -10$ and -25 lies a broad island of intensity, which might be the mergence of the lowest modes of both branches. On the right edge, over $m = 100$, artifacts congregate.

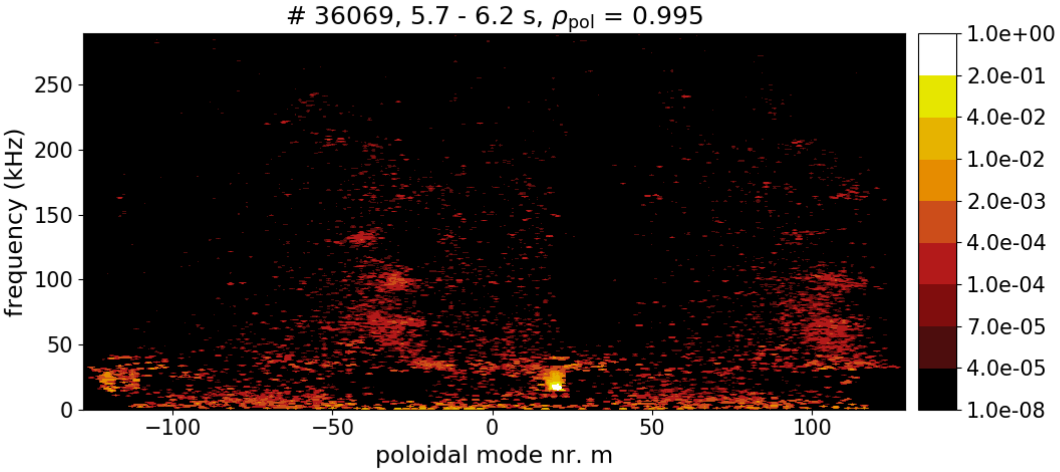

Figure 5.17: Poloidal mode number histogram of #36069 applying $\rho_{\mathrm{pol}} = 0.995$. The core mode mistakenly appears at $m = 20$. A steep branch of four modes appears. Intensity below suggests a flat branch. On the right, artifacts are visible.

The results of the fits are seen in figure 5.18. In the steep branch, the slope is -3.70 ± 0.38 kHz and the offset is -18.69 kHz. Fits for the intensity below, at the frequencies corresponding to the flat branch of figure 5.16, indeed converge. However, these results must be treated with caution, as the modes do not line up nicely. The flat branch has a slope of -2.46 ± 0.42 kHz and an offset of -15.33 kHz. Mode numbers and frequencies of the modes are listed in table 5.13.

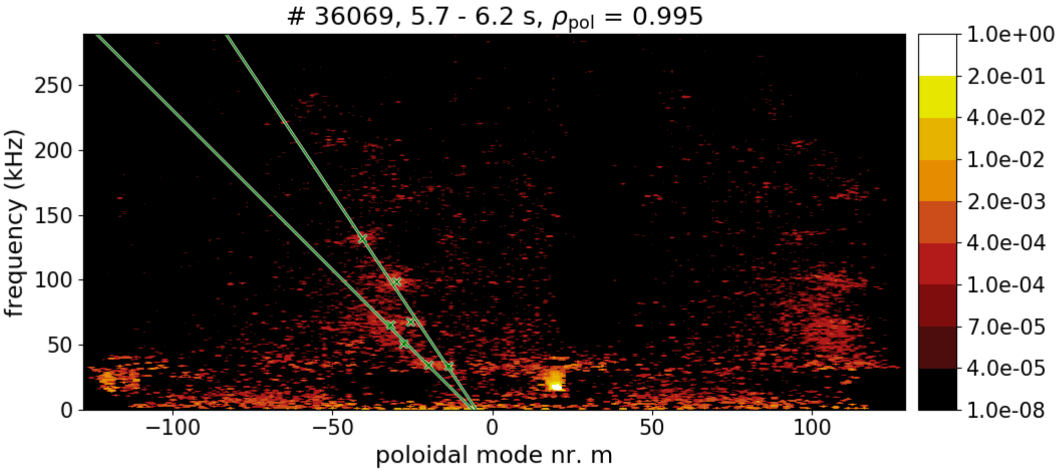

Figure 5.18: Poloidal mode number histogram of #36069 with $\rho_{\text{pol}} = 0.995$. The modes and branches are identified with green crosses and green lines.

mode	n	f (kHz)
branch 1		
1	-13.67	33.8
2	-25.53	67.8
3	-30.06	98.9
4	-40.79	131.8
branch 2		
1	-19.86	34.5
2	-27.95	50.5
3	-32.07	65.6

Table 5.13: Modes in the m histogram of #36069, $\rho_{\text{pol}} = 0.995$ with mode numbers and frequencies.

In figure 5.19, the q profile of #36069 is indicated as green triangles. It is seen together with m/n for the steep branch as purple circles with error bars and m/n for the flat as branch orange squares with error bars. The mode determination is done at $\rho_{\mathrm{pol}} = 0.94$, 0.98 and 0.995. All values can be found in table 5.14. For the steep branch, the conclusion is once more that the modes are localized outside of $\rho_{\mathrm{pol}} = 0.995$. The flat branch could stem from a position inside $\rho_{\mathrm{pol}} = 0.995$, as its confidence interval overlaps with the profile.

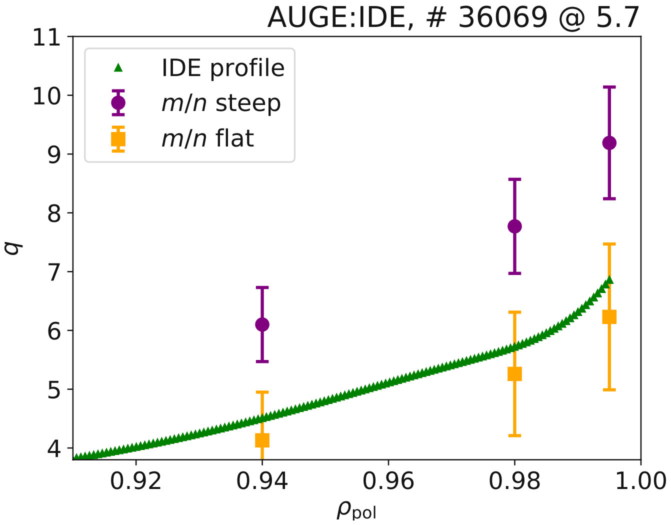

Figure 5.19: Safety factor over flux coordinate for #36069. The green triangles indicate the profile from IDE, the purple circles with error bars show m/n for the steep branch and the orange squares with error bars are the m/n values for the flat branch.

ρ_{pol}	m/n steep	m/n flat	q
0.94	6.10 ± 0.63	4.13 ± 0.82	4.51
0.98	7.77 ± 0.80	5.26 ± 1.05	5.72
0.995	9.19 ± 0.95	6.23 ± 1.24	6.86

Table 5.14: Values of q from IDE, along with m/n at each position for both branches in #36069.

Mode velocities for both of the branches are calculated and plotted over ρ_{pol} in figure 5.20. The velocity of the steep branch is shown as a purple line with violet uncertainty and that of the flat branch is shown as an orange line with dark orange uncertainty. They are compared to v_{ExB} from EER as green circles and the electron diamagnetic velocity as a blue line with cyan uncertainty. Unfortunately, no error estimates could be computed for the v_{ExB} data from EER in this discharge. The velocity of the flat branch can be explained by the combination of v_{ExB} and the electron diamagnetic velocity near the edge. Its large uncertainty reflects the f/n uncertainty in this branch. For the steep branch, the observation matches that of #36068, where no drift velocity comes close to explaining it.

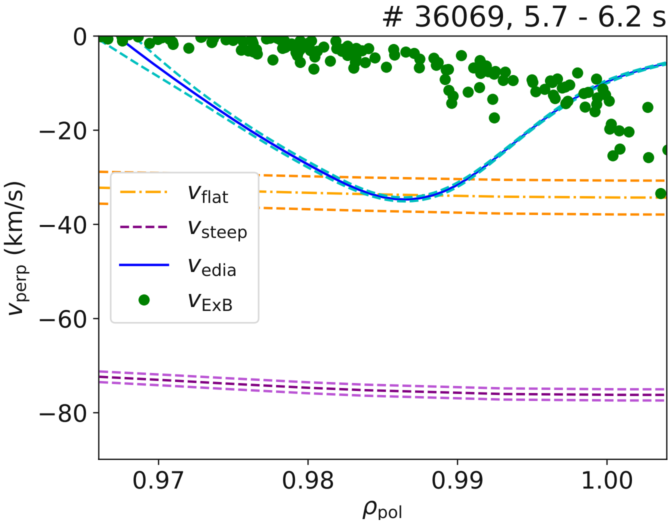

Figure 5.20: Comparison of velocity profiles over flux coordinate for #36069. Green circles with error bars depict v_{ExB}, the blue line with cyan uncertainty shows the electron diamagnetic velocity, the purple line with violet uncertainty is the mode velocity of the steep branch and the orange line with dark orange uncertainty is that of the flat branch.

To evaluate the data from EER, they are compared to HES results as well as the ion diamagnetic velocity based on chapter 4.3. Empirical evidence suggests that near the plasma edge, the absolute values of v_{ExB} and ion diamagnetic velocity are close to equal. [36] In that case, the ion fluid is in an equilibrium where the residual velocity is zero.

Figure 5.21 compares v_{ExB} from EER as green circles and from HES as black squares with error bars to the ion diamagnetic velocity as a red line with rose uncertainty. For visual comparability, the v_{ExB} values are plotted into positive v_{perp}. There is disagreement in particular between the CXRS data and the ion diamagnetic velocity. The HES data suggest a shape that is somewhat reminiscent of the descent in the right of the red curve. However, its absolute values are mostly lower than $v_{\mathrm{i,dia}}$, with a possible intersection near $\rho_{\mathrm{pol}} = 0.98$. Even when assuming a larger electric field, such that v_{ExB} is nearly $v_{\mathrm{i,dia}}$, the drifts cannot explain the fastest mode velocity.

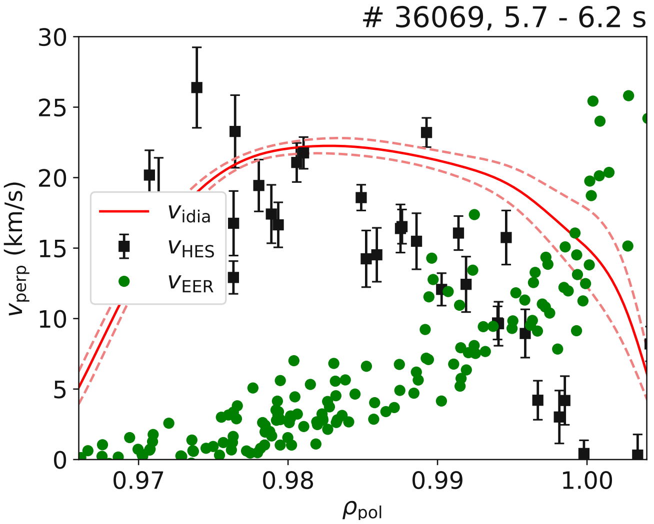

Figure 5.21: Comparison of v_{ExB} from EER as green circles and from HES as black squares with error bars to the ion diamagnetic velocity as a red line with rose uncertainty. Plot over flux coordinate for #36069.

5.4 #36327

Discharge #36327 is characterized by fast gas puff modulation with deuterium gas. It shows type-I ELMs. The heating is done with ECRH and, to a lesser extent, NBI. q_{95} varies throughout the discharge, but averages about 4.45 in the considered time window. It stretches from 2.5 s to 4.0 s. All parameters are covered in table 5.15.

B_{tor}	$-2.500\,\mathrm{T}$
I_{plasma}	$0.989\,\mathrm{MA}$
q_{95}	≈ 4.45
P_{ECRH}	$3.968\,\mathrm{MW}$
P_{NBI}	$2.538\,\mathrm{MW}$

Table 5.15: Parameters of #36327.

Figure 5.22 shows the toroidal mode number histogram of #36327. The core mode sits at low frequency. In a steep mode branch, modes from $n = -1$ to -9 appear. They are fairly aligned except for $n = -9$, while other modes seem stretched out and might be comprised of separate maxima. Modes with $n = -4$ to -6 produce artifacts in the right half of the figure, at around 140 kHz. Below the steep branch, there are more modes. Not all of them can be assigned to one flat branch, but seem to be part of several alignments.

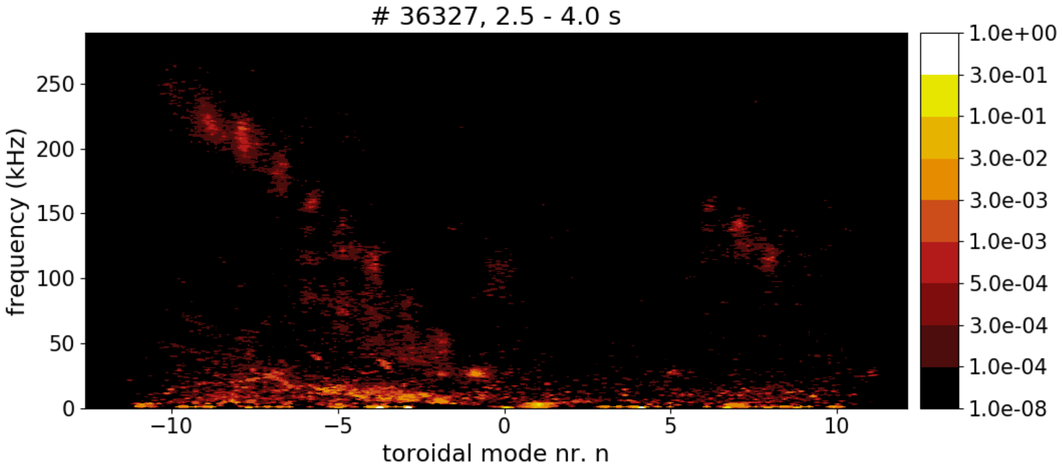

Figure 5.22: Toroidal mode number histogram of #36327. The core mode lies at low frequency. Modes down to $n = -9$ can be identified. On the right, artifacts of $n = -4$ to -6 are visible. Below the steepest branch, more modes are situated.

Modes are marked in figure 5.23. A steep branch is drawn through modes $n = -1$ to $n = -8$. It results in a slope of -27.37 ± 0.53 kHz and an offset of 1.82 kHz. Furthermore, a branch is fitted through four of the lowest possible modes. This flat branch has a slope of -15.34 ± 0.65 kHz and an offset of -2.15 kHz. All the marked modes are listed in table 5.16.

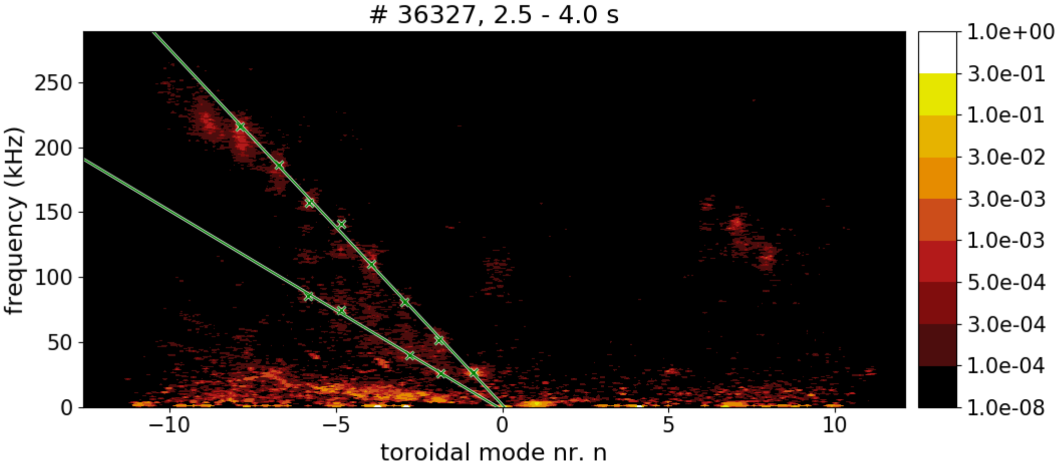

Figure 5.23: Toroidal mode number histogram of #36327. The modes and branches are identified with green crosses and green lines.

mode	n	f (kHz)
branch 1		
1	-0.86	26.6
2	-1.91	51.3
3	-2.94	80.5
4	-3.94	110.0
5	-4.84	140.8
6	-5.80	157.3
7	-6.71	186.9
8	-7.88	215.6
branch 2		
1	-1.87	26.3
2	-2.80	40.3
3	-4.86	74.6
4	-5.84	85.8

Table 5.16: Modes in the n histogram of #36327 with mode numbers and frequencies.

The respective poloidal mode number histogram of #36327 with $\rho_{\mathrm{pol}} = 0.995$ can be seen in figure 5.24. Apart from the core mode, one intense mode at around $m = -15$ and 25 kHz is visible. There are two more apparent, rather wide modes between 100 and 150 kHz, which have artifacts on the right. Unfortunately, not all modes from figure 5.22 can be distinguished in figure 5.24, as some might be merged together. Only the distribution of the lowest branch can be recognized.

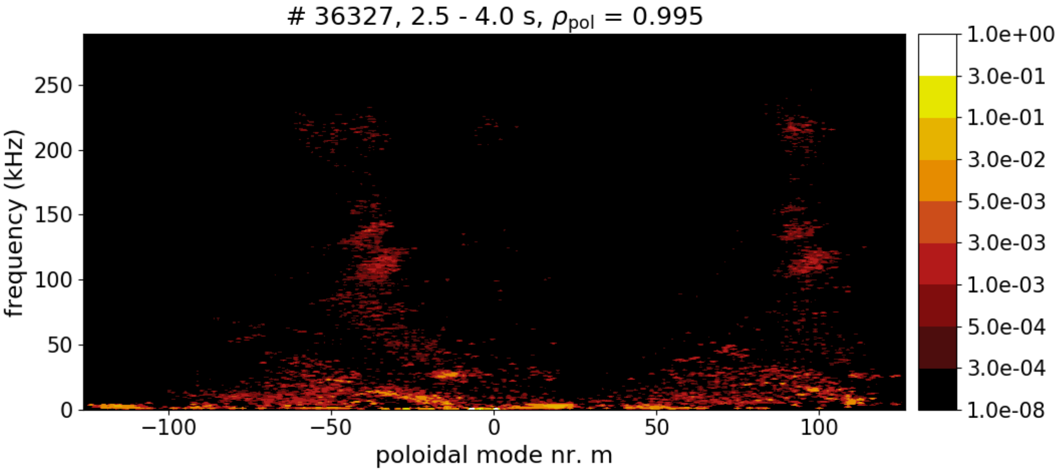

Figure 5.24: Poloidal mode number histogram of #36327 applying $\rho_{\mathrm{pol}} = 0.995$. Apart from the core mode, there is one intense mode at 25 kHz and two wide modes between 100 and 150 kHz. The distribution of the lowest branch can be recognized. On the right, artifacts are visible.

Figure 5.25 contains the fits. A steep branch of three modes is indicated, which has a slope of -4.30 ± 0.43 kHz and an offset of -34.44 kHz. The flatter branch is also fitted through only three modes and shows a slope of -1.97 ± 0.14 kHz and an offset of -1.43 kHz. It also passes through the intense mode at 25 kHz, implying that this structure might be comprised of two modes directly overlaid. All distinctly identified modes are held in table 5.17.

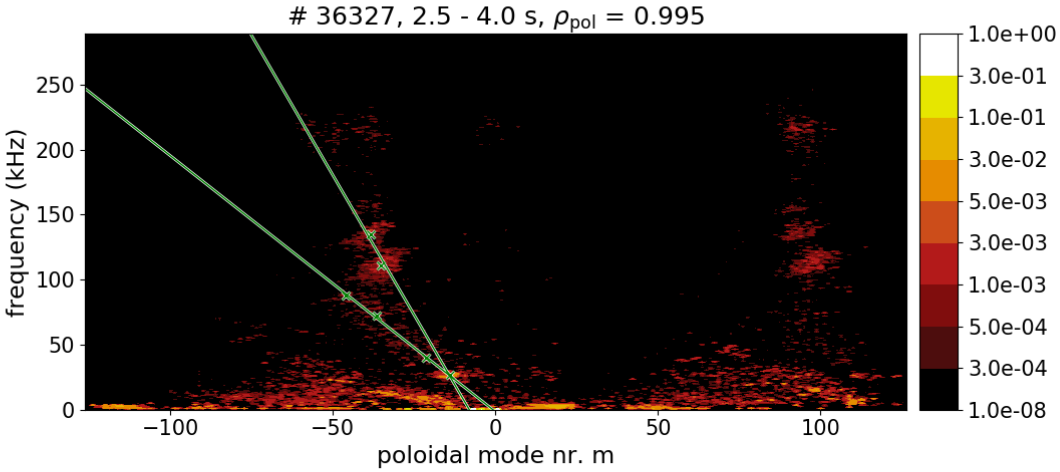

Figure 5.25: Poloidal mode number histogram of #36327 with $\rho_{\mathrm{pol}} = 0.995$. The modes and branches are identified with green crosses and green lines.

mode	n	f (kHz)
branch 1		
1	-14.05	26.7
2	-35.21	110.8
3	-38.20	134.9
branch 2		
1	-21.52	40.2
2	-36.49	72.3
3	-45.91	87.7

Table 5.17: Modes in the m histogram of #36327, $\rho_{\mathrm{pol}} = 0.995$ with mode numbers and frequencies.

Figure 5.26 shows the q profile of #36327 with green triangles. The steep branch is indicated as purple circles with error bars has lower m/n values than the flat branch, which is shown as orange squares with error bars. Mode numbers are evaluated at $\rho_{\mathrm{pol}} = 0.94$, 0.98 and 0.995. The respective m/n and q results are held in table 5.18. Both branches seem to be localized outside of $\rho_{\mathrm{pol}} = 0.995$ because their m/n lies above the q profile. However, the steeper branch could lie very closely outside, taking the uncertainty interval into account.

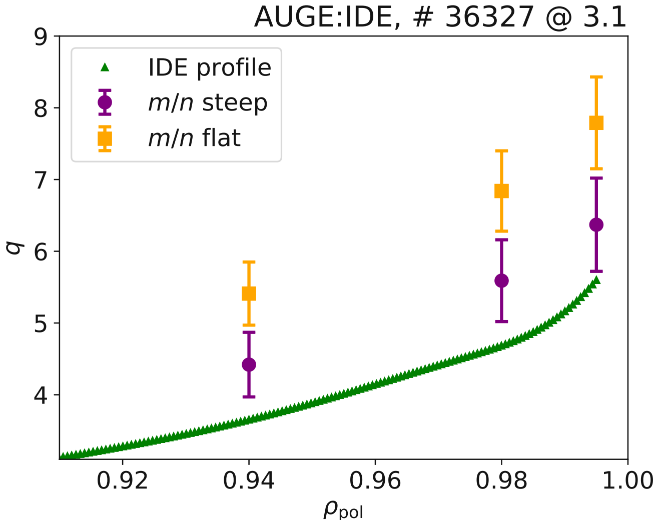

Figure 5.26: Safety factor over flux coordinate for #36327. The green triangles indicate the profile from IDE, the purple circles with error bars show m/n for the steep branch and the orange squares with error bars are the m/n values for the flat branch.

ρ_{pol}	m/n steep	m/n flat	q
0.94	4.42 ± 0.45	5.41 ± 0.44	3.65
0.98	5.59 ± 0.57	6.84 ± 0.56	4.68
0.995	6.37 ± 0.65	7.79 ± 0.64	5.60

Table 5.18: Values of q from IDE, along with m/n at each position for both branches in #36327.

The comparison of velocities is depicted in figure 5.27. v_{ExB} from EER is shown as green circles with error bars and the electron diamagnetic velocity as a blue line with cyan uncertainty, the velocity of the steep branch is shown as a purple line with violet uncertainty and that of the flat branch as an orange line with dark orange uncertainty. Due to the long time interval from 2.5 to 4 s in this discharge, EER data points appear in a large quantity and considerably scattered. As for the flat branch, it could move with the combination of v_{ExB} and electron diamagnetic velocity. The steep branch seems to move faster than the drifts.

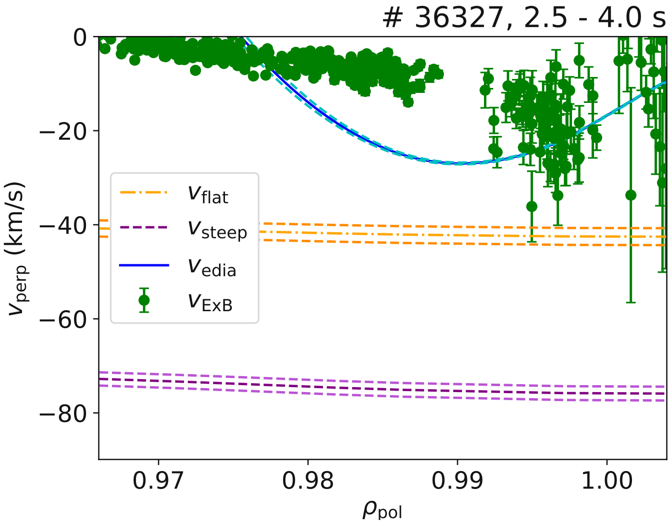

Figure 5.27: Comparison of velocity profiles over flux coordinate for #36327. Green circles with error bars depict v_{ExB}, the blue line with cyan uncertainty shows the electron diamagnetic velocity, the purple line with violet uncertainty is the mode velocity of the steep branch and the orange line with dark orange uncertainty is that of the flat branch.

5.5 #36650

The list of discharges is concluded by #36650 with low power separatrix fuelling seeding. It sports a type-I ELM regime in a long, stable phase. Table 5.19 shows the parameters of the discharge. A time window from 3.0 s to 4.5 s is regarded.

B_{tor}	$-2.520\,\mathrm{T}$
I_{plasma}	$0.997\,\mathrm{MA}$
q_{95}	4.253
P_{ECRH}	$2.627\,\mathrm{MW}$
P_{NBI}	$3.108\,\mathrm{MW}$

Table 5.19: Parameters of #36650.

The toroidal mode number histogram of the discharge is presented in figure 5.28. At $n = 1$ sits the core mode. Two very clear branches can be seen, with five modes each. Even the steeper of the branches ends under 150 kHz. No artifacts of strong intensity are visible.

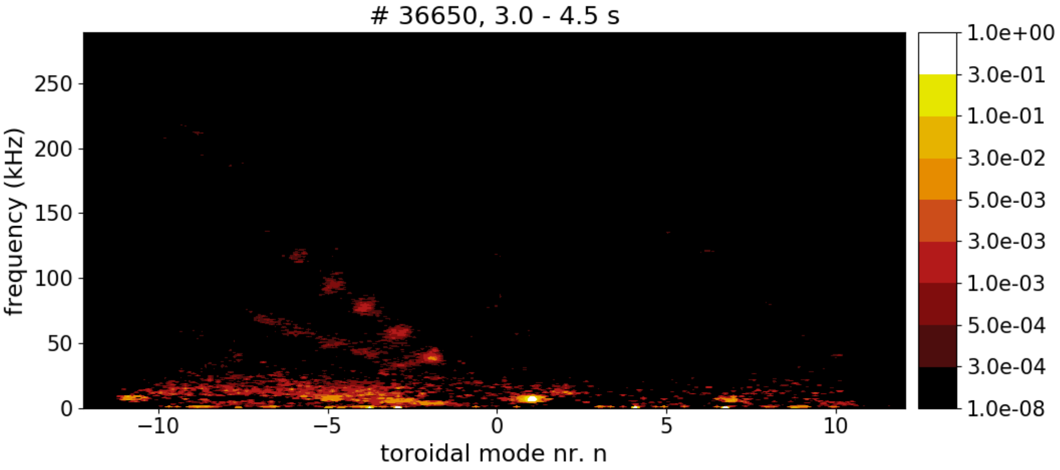

Figure 5.28: Toroidal mode number histogram of #36650. At $n = 1$ sits the core mode. There are two branches of five modes each. No artifacts of strong intensity are visible.

These branches are tagged in figure 5.29. Due to the clear delimitation of the modes, all of them can be fitted easily. The steep branch has a slope of $-19.52 \pm 0.37\,\text{kHz}$ and an offset of $1.15\,\text{kHz}$. The slope of the flat branch is $-8.92 \pm 0.27\,\text{kHz}$, while its offset is $8.00\,\text{kHz}$. Table 5.20 contains the mode numbers and frequencies of the described modes.

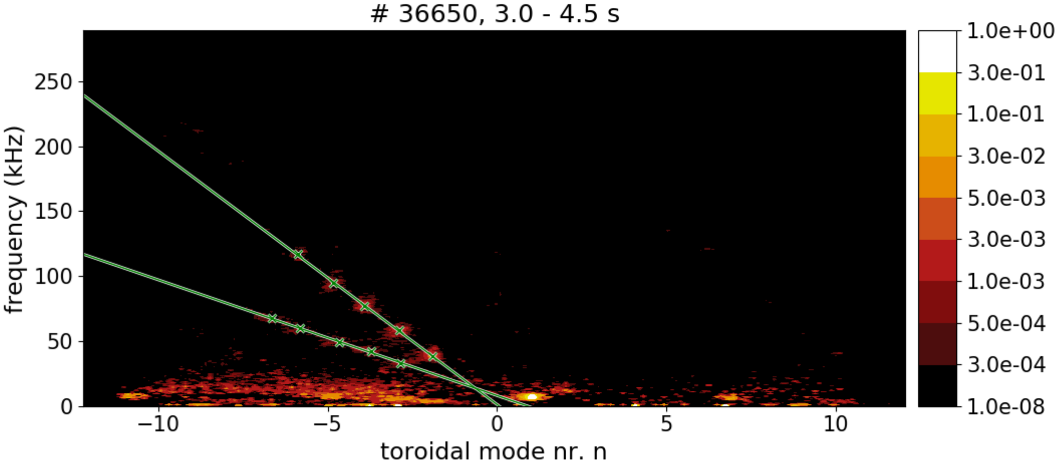

Figure 5.29: Toroidal mode number histogram of #36650. The modes and branches are identified with green crosses and green lines.

mode	n	f (kHz)
branch 1		
1	-1.92	38.7
2	-2.88	58.1
3	-3.93	77.2
4	-4.84	94.4
5	-5.88	117.1
branch 2		
1	-2.86	32.9
2	-3.72	42.3
3	-4.65	49.1
4	-5.83	59.6
5	-6.65	67.5

Table 5.20: Modes in the n histogram of #36650 with mode numbers and frequencies.

Figure 5.30 holds the poloidal mode number histogram of #36650 with $\rho_{\text{pol}} = 0.995$. It shows the key features from figure 5.28, with a core mode mistakenly appearing between $m = 15$ and 20. Four modes of the steep branch can be distinguished, while the fifth, topmost, is missing from the line. However, at the respective frequency, there is intensity around $m = -40$ and an artifact on the right side of the figure. All the modes from the flat branch are rather well discernible.

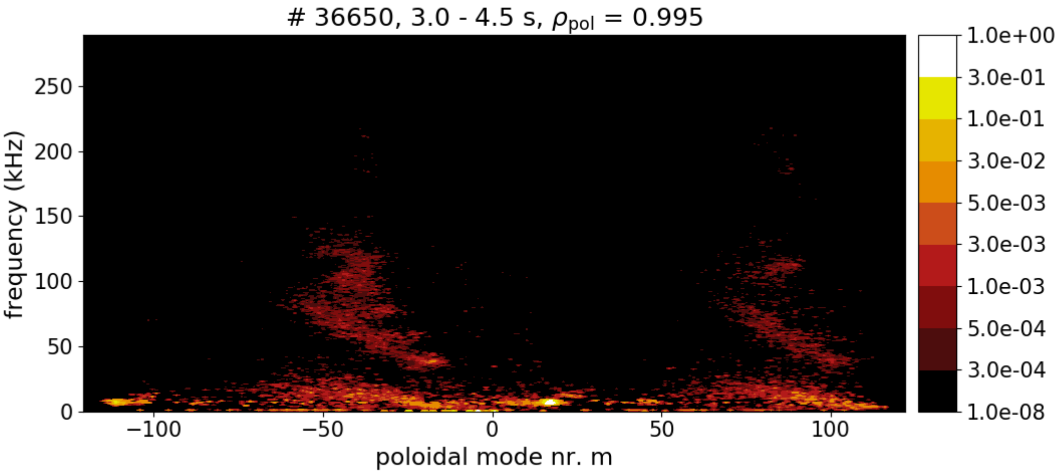

Figure 5.30: Poloidal mode number histogram of #36650 with $\rho_{\text{pol}} = 0.995$. The core mode and four modes of the steep branch can be seen, the fifth is somewhat displaced. All modes of the flat branch are in place.

Shown in figure 5.31 are the marked branches of #36650. The steep branch, consisting of four modes, has a slope of $-2.62 \pm 0.18\,\mathrm{kHz}$ and an offset of $-5.84\,\mathrm{kHz}$. Five other modes contributing to the flat branch result in a slope of $-1.30 \pm 0.04\,\mathrm{kHz}$ and an offset of $10.34\,\mathrm{kHz}$. A summary of these modes is in table 5.21.

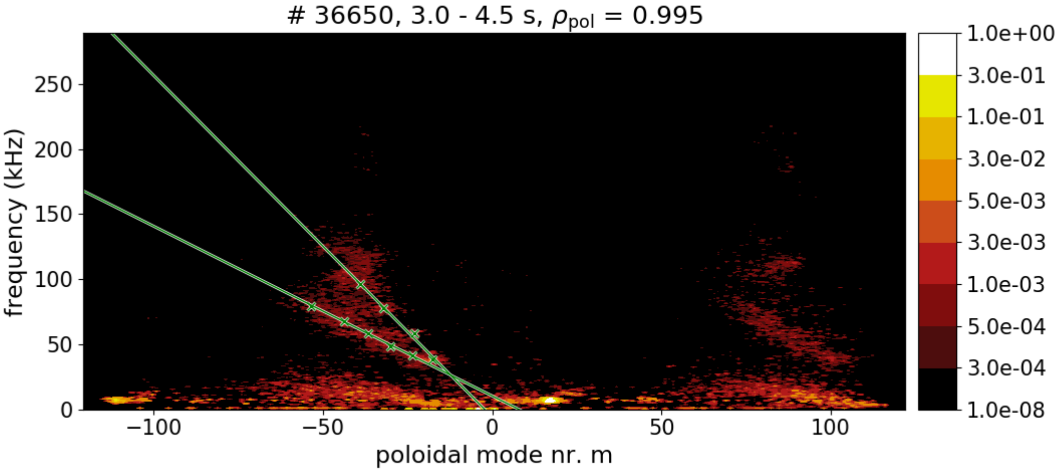

36650, 3.0 - 4.5 s, ρ_{pol} = 0.995

Figure 5.31: Poloidal mode number histogram of #36650 with $\rho_{\mathrm{pol}} = 0.995$. The modes and branches are identified with green crosses and green lines.

mode	n	f (kHz)
branch 1		
1	-17.68	38.3
2	-23.12	58.3
3	-32.26	77.7
4	-39.10	96.6
branch 2		
1	-23.60	41.2
2	-30.00	48.4
3	-36.50	58.8
4	-43.60	68.0
5	-53.40	79.3

Table 5.21: Modes in the m histogram of #36650, $\rho_{\mathrm{pol}} = 0.995$ with mode numbers and frequencies.

A q profile for the discharge #36650 is given in figure 5.32. The IDE data of q are shown as green triangles, m/n of the steep branch as purple circles with error bars and that of the flat branch as orange squares with error bars. The mode determination is performed at $\rho_{\mathrm{pol}} = 0.94$, 0.98 and 0.995. All values can be seen in table 5.22. In this case once more, the results based on mode numbers exceed the profile clearly for both branches. A localization close to the separatrix and outside of $\rho_{\mathrm{pol}} = 0.995$ seems likely. Unlike in the other discharges, the uncertainties of each branch clearly overlap, so a localization on the same flux surface is possible. This result is interesting because the branches move with distinct velocities.

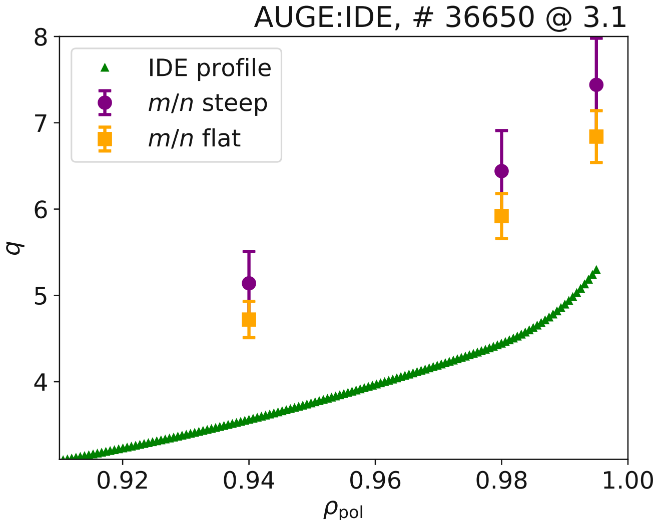

Figure 5.32: Safety factor over flux coordinate for #36650. The green triangles indicate the profile from IDE, the purple circles with error bars show m/n for the steep branch and the orange squares with error bars are the m/n values for the flat branch.

ρ_{pol}	m/n steep	m/n flat	q
0.94	5.14 ± 0.37	4.72 ± 0.21	3.56
0.98	6.44 ± 0.47	5.92 ± 0.26	4.44
0.995	7.44 ± 0.54	6.84 ± 0.30	5.29

Table 5.22: Values of q from IDE, along with m/n at each position for both branches in #36650.

Figure 5.33 compares velocities in the pedestal of discharge #36650. Green circles with error bars depict v_{ExB} from EER, the blue line with cyan uncertainty shows the electron diamagnetic velocity, the purple line with violet uncertainty is the mode velocity of the steep branch and the orange line with dark orange uncertainty is that of the flat branch. Strong scattering appears in the EER data, like in discharge #36327. The flat branch could move with the combination of v_{ExB} and electron diamagnetic velocity, or even v_{ExB} alone. Three outlying EER data points reach the velocity of the steep branch. It seems that the combination of the drifts could potentially account for the mode velocity of the steep branch in this case, depending on the real v_{ExB} value.

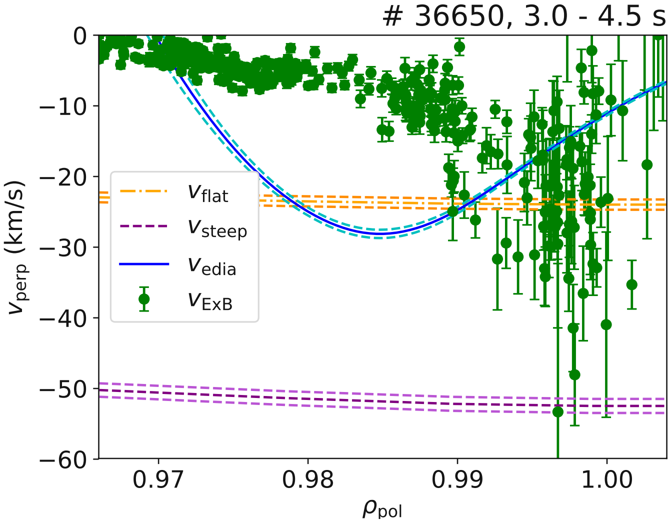

Figure 5.33: Comparison of velocity profiles over flux coordinate for #36650. Green circles with error bars depict v_{ExB}, the blue line with cyan uncertainty shows the electron diamagnetic velocity, the purple line with violet uncertainty is the mode velocity of the steep branch and the orange line with dark orange uncertainty is that of the flat branch.

Chapter 6

Conclusion and outlook

In this final chapter, an attempt is made to construct a physical picture for the nature of the observed modes. This is a conjecture in the scope of the experimental results presented in the previous chapter. The results are being reviewed and an outlook to possible future research is given.

First of all, the instability that drives the modes shall be identified based on the MHD stability consideration in chapter 2.2. The destabilizing contributions in equation 2.21 are the ballooning instability, which depends on the field line curvature and therefore only appears on the low field side, and the peeling instability. Ballooning modes are pressure driven and dependent on the pressure gradient, peeling modes are current driven.

It is natural to expect the mode locality where the strongest magnitude of its driving cause is. As part of the calculation of diamagnetic velocities presented in chapter 4.3, ion- and electron pressure profiles are obtained. They show a peak gradient normally near the pedestal top, at $\rho_{\text{pol}} = 0.98$, except for #36327, where the electron pressure is maximized around $\rho_{\text{pol}} = 0.99$. This would indicate the expected locality for ballooning modes. However, the mode localization for the discharges presented in this thesis consistently yields $\rho_{\text{pol}} > 0.995$, except maybe for the flat branch in # 36069. So close to the separatrix, the pressure has fallen off considerably. To add to this, frequencies associated with the modes are mostly also picked up by coils at the high field side. As the ballooning instability is not prevalent at the high field side, their appearance would be unexpected. Hence, an identification as current driven, peeling modes seems more likely.

The mode localization itself is unsatisfactory since agreement according to 1.9 could mostly not be established or at least not be linked to a specific position. However, the following paragraph elaborates on why a range from $\rho_{\text{pol}} = 0.995$ to the separatrix is most likely for the localization in cases where $q < m/n$ is found.

Deep inside the plasma, the cross section of flux surfaces is near circular, with no expressed x-point. In this condition, the straight field line angle $\theta*$ of poloidal coil positions scales nearly linearly with the safety factor. This directly affects the determined poloidal mode numbers, which makes precise localization difficult, as the calculated m/n changes almost parallelly to the q profile. Towards the separatrix, the safety factor diverges caused by the x-point, which lies away from the positions of the used coils. Very near the plasma edge, the safety factor q is therefore expected to rise steeper than the determined m/n and create an intersecting point between both values. In addition, the relative difference m/nq often slightly decreases towards the separatrix in the presented discharges. This implies a localization between $\rho_{\text{pol}} = 0.995$ and the separatrix for the considered cases. Unfortunately, IDE does not resolve this inferred position on the q profile.

As a raw approximation, the flux coordinate ρ_{pol} can be converted linearly to the minor radius. Since the minor radius of ASDEX Upgrade extends to about 0.6 m, the gap from $\rho_{\text{pol}} = 0.995$ to the separatrix amounts to 3 mm. That is a measure for the precision of the localization.

An offset is apparent in poloidal mode numbers in a lot of branches. Typically, it is negative, meaning that the branch lies to the left of the origin crossing in the histogram. This leaves the localization with an ambiguity on whether to consider the slopes f/m and f/n, or individual mode numbers. All m/n values in this thesis follow from the quotient of slopes. By instead using mode numbers of individual modes to calculate m/n, the values would differ within a branch. That would contradict the existence of a single, localized structure, while the constant f/n values with little offset in most branches affirms it. Furthermore, due to the more negative m values, m/n would lie even further from agreement with the safety factor, than in the shown examples. The application of slopes in the localization seems more suitable.

Ideal, non-resistive plasma conditions can offset the appearance of mode localities, as detailed in chapter 2.3. The magnetic signal of the mode then appears where the plasma is resistive. While ideal conditions might be present at the actual locality of the modes, it is unlikely that they account for a large deviation in the localization.

Plasma resistivity scales with electron temperature according to equation 2.22. This indicates a steep incline of resistivity at the plasma edge. Assuming a mode localization in the pedestal, the gap to a resistive position and thus the shift in m can only be small. Ideal modes might change the apparent poloidal mode number, but provide no specific reasoning for a constant offset in m.

The most pressing discrepancy is between the mode velocity in steep branches and the respective plasma drifts, whereas the velocity of flat mode branches seen in #36969, #36327 and #36650 can easily be explained by the combination of $\vec{v}_{\mathrm{ExB}}$ and the electron diamagnetic velocity. An exception is maybe formed by #36650, where $\vec{v}_{\mathrm{ExB}}$ reaches close to the steep branch. However, the EER data of #36650 scatter greatly and their error bars are partly large, with the bulk of values being much lower. Furthermore, EER results for #36069 must be treated with extra caution as they lack error estimates. Their reliability is discussed in relation to HES data in figure 5.21.

Any arguments concerning the poloidal mode number are irrelevant here, as it is not included in the velocity calculation. Ideal modes do not provide an explanation for the additional phase velocity. The measured quantity on which the velocity calculation is based is the mode frequency. While a velocity purely perpendicular to the magnetic field is assumed in equation 4.5, any additional parallel velocity component would contribute to the measured frequency as well. Parallel velocity is associated with Alfvén waves, their velocity is given by equation 2.24. For instance, at a density of around $n = 10^{19}\,\mathrm{m}^{-3}$, this yields $10\,000\,\mathrm{km\,s}^{-1}$. The Alfvén frequency can be calculated based on equation 2.25. In the presented discharges, it lies between 20 and 40 kHz in the pedestal.

The resulting frequency follows from a superposition with the plasma drifts. When viewing the mode motion in a frequency picture, the aforementioned discrepancy is between the drift-induced frequencies and f/n of the steep branches. The Alfvén frequency is in the right range to bridge the discrepancy which offers a possibility to explain the observed frequencies. Perpendicular and parallel velocity components may amplify or counteract each other in the measured frequency, based on their signs. For the amplifying effect expected for the presented cases, Alfvén waves must move along field lines against the $\vec{B}$ vector, superimposing the counter-current direction of the drifts.

According to [26], Alfvén waves can deviate from equation 1.9, resulting in a constant offset in mode numbers. This is perhaps the best explanation for the offset in poloidal mode numbers of branches.

As for the flat branches, an explanation as purely drifting modes without parallel velocity suffices. One interpretation is that these flat branches are indeed current driven MHD modes, which excite Alfvén waves at resonant mode numbers and higher frequencies. While this is a tempting conclusion, there is the problem that flat branches are absent in #33211 and #36068. To add to this, the flat branches in #36069 and #36327 end at lower mode numbers than their respective steep branches.

Interestingly, there is a conspicuous jump in poloidal mode number branches, always appearing between 140 and 150 kHz. Above that frequency, the branch might fade or continue with a parallel shift. The phenomenon is limited to steep branches because none of the flat branches reaches this frequency. The reproducibility of this discontinuity in various discharges might hint at a measurement artifact, possibly originating in the electronics. However, in [26], a gap in the continuous spectrum of so-called TAEs (toroidicity induced Alfvén eigenmodes) is mentioned, which seems to appear between 140 and 150 kHz at ASDEX Upgrade. This coincidence might explain the jump. However, the mathematical treatment of TAEs is beyond the scope of this thesis.

It is for these reasons that the image of modes being carried with drifts alone must be revised. To gain a deeper understanding of the discussed phenomena, they must be observed under changed parameters. Different heating mechanisms help to pinpoint the influences on the mode formation and their frequency. Similar projects on other machines would be of interest to compare the localization and velocity calculation results.

In a recent 2021 paper, modes in the pedestal of the DIII-D TOKAMAK are investigated. These modes show deviating structure, with one toroidal mode number, for instance $n = 3$, associated with several poloidal mode numbers like $m = 15, 16, 17, 18$. The paper concludes that they are microtearing modes, their frequency is found to be consistent with the electron diamagnetic drift at DIII-D. [37]

Since the `mode_determination.py` program allows to deselect individual coils, the effect of different coil arrays can be tested. Their effect on detected artifacts is discussed in chapter 4.1.3. Generally, no novel mode structures are observed upon deselection of coils. A higher mode number resolution can be obtained through more closely sitting pick-up coils.

For comparison with drift velocities, discharges with good CXRS data are needed. This is often the limiting factor, since the calculation of electric fields from CXRS is intricate. The selection of discharges in this thesis was ruled by this.

Bibliography

[1] Hannah Ritchie and Max Roser. “Energy”. In: *Our World in Data* (2020). https://ourworldindata.org/energy.

[2] D. Feldman, W. Collins, and P. Gero. “Observational determination of surface radiative forcing by CO2 from 2000 to 2010”. In: *Nature* 519 (2015), pp. 339–343. DOI: `10.1038/nature14240`.

[3] D. Qing et al. *The River Dragon Has Come!: Three Gorges Dam and the Fate of China’s Yangtze River and Its People*. Taylor & Francis, 2016. ISBN: 9781315502762. URL: `https://books.google.at/books?id=nX6TDAAAQBAJ`.

[4] Allan Drewitt and R. Langston. “Collision Effects of Wind-power Generators and Other Obstacles on Birds”. In: *Annals of the New York Academy of Sciences* 1134 (June 2008), pp. 233–266. DOI: `10.1196/annals.1439.015`.

[5] Frank Dimroth. *New world record for solar cell efficiency at 46 - French-German cooperation confirms competitive advantage of European photovoltaic industry*. 2014. URL: `https://www.ise.fraunhofer.de/en/press-media/press-releases/2014/new-world-record-for-solar-cell-efficiency-at-46-percent.html` (visited on 06/10/2021).

[6] B. Baltes et al. “Präzisierung und Weiterentwicklung der Sicherheitskriterien für die Endlagerung radioaktiver Abfälle in einem Bergwerk”. Gesellschaft für Reaktorsicherheit Köln, 2002. unpublished.

[7] C. Van Der Leun and C. Alderliesten. “The deuteron binding energy”. In: *Nuclear Physics A* 380.2 (1982), pp. 261–269. ISSN: 0375-9474. DOI: `https://doi.org/10.1016/0375-9474(82)90105-1`. URL: `https://www.sciencedirect.com/science/article/pii/0375947482901051`.

[8] N. Ghahramany, S. Gharaati, and M. Ghanaatian. “New approach to nuclear binding energy in integrated nuclear model”. In: *Journal of Theoretical and Applied Physics* 6 (2012). DOI: `https://doi.org/10.1186/2251-7235-6-3`.

[9] H.-S Bosch and G.M Hale. “Improved formulas for fusion cross-sections and thermal reactivities”. In: *Nuclear Fusion* 32.4 (Apr. 1992), pp. 611–631. DOI: `10.1088/0029-5515/32/4/i07`. URL: `https://doi.org/10.1088/0029-5515/32/4/i07`.

[10] H. J. de Blank. “Guiding Center Motion”. In: *Fusion Science and Technology* 49.2T (2006), pp. 59–66. DOI: `10.13182/FST06-A1104`. eprint: `https://doi.org/10.13182/FST06-A1104`. URL: `https://doi.org/10.13182/FST06-A1104`.

[11] Max Planck Institute for Plasma Physics. *Online picture archive*. URL: `https://www.ipp.mpg.de/1471827/asdex_upgrade?page=1` (visited on 06/16/2021).

[12] van Milligen, Boudewijn. *Toroidal coordinates*. URL: `http://fusionwiki.ciemat.es/wiki/Toroidal_coordinates` (visited on 06/14/2021).

[13] Harmut Zohm. *Magnetohydrodynamic Stability of Tokamaks*. Wiley-VCH, 2015. ISBN: 978-3-527-41232-7.

[14] Alexander Felician Mink. “Structure and Nonlinear Development of Edge Localized Magnetohydrodynamic Instabilities on the ASDEX Upgrade Tokamak”. dissertation. Technical University Munich, 2018.

[15] F. Wagner et al. “Regime of Improved Confinement and High Beta in Neutral-Beam-Heated Divertor Discharges of the ASDEX Tokamak”. In: *Phys. Rev. Lett.* 49 (19 Nov. 1982), pp. 1408–1412. DOI: `10.1103/PhysRevLett.49.1408`. URL: `https://link.aps.org/doi/10.1103/PhysRevLett.49.1408`.

[16] J W Connor and H R Wilson. “A review of theories of the L-H transition”. In: *Plasma Physics and Controlled Fusion* 42.1 (Dec. 1999), R1–R74. DOI: `10.1088/0741-3335/42/1/201`. URL: `https://doi.org/10.1088/0741-3335/42/1/201`.

[17] H Zohm. “Edge localized modes (ELMs)”. In: *Plasma Physics and Controlled Fusion* 38.2 (Feb. 1996), pp. 105–128. DOI: `10.1088/0741-3335/38/2/001`. URL: `https://doi.org/10.1088/0741-3335/38/2/001`.

[18] P. Gohil et al. “Study of Giant Edge-Localized Modes in DIII-D and Comparison with Ballooning Theory”. In: *Phys. Rev. Lett.* 61 (14 Oct. 1988), pp. 1603–1606. DOI: `10.1103/PhysRevLett.61.1603`. URL: `https://link.aps.org/doi/10.1103/PhysRevLett.61.1603`.

[19] S.-I Itoh, K Itoh, and A Fukuyama. “The ELMy H mode as a limit cycle and the transient responses of H modes in tokamaks”. In: *Nuclear Fusion* 33.10 (Oct. 1993), pp. 1445–1457. DOI: `10.1088/0029-5515/33/10/i04`. URL: `https://doi.org/10.1088/0029-5515/33/10/i04`.

[20] J. W. Connor et al. “Magnetohydrodynamic stability of tokamak edge plasmas”. In: *Physics of Plasmas* 5.7 (1998), pp. 2687–2700. DOI: `10.1063/1.872956`. eprint: `https://doi.org/10.1063/1.872956`. URL: `https://doi.org/10.1063/1.872956`.

[21] P Manz et al. “Velocimetry analysis of type-I edge localized mode precursors in ASDEX Upgrade”. In: *Plasma Physics and Controlled Fusion* 56.3 (Feb. 2014), p. 035010. DOI: `10.1088/0741-3335/56/3/035010`. URL: `https://doi.org/10.1088/0741-3335/56/3/035010`.

[22] J. A. Morales et al. “Edge localized mode rotation and the nonlinear dynamics of filaments”. In: *Physics of Plasmas* 23.4 (2016), p. 042513. DOI: 10.1063/1.4947201. eprint: https://doi.org/10.1063/1.4947201. URL: https://doi.org/10.1063/1.4947201.

[23] M Willensdorfer et al. “Plasma response measurements of external magnetic perturbations using electron cyclotron emission and comparisons to 3D ideal MHD equilibrium”. In: *Plasma Physics and Controlled Fusion* 58.11 (Sept. 2016), p. 114004. DOI: 10.1088/0741-3335/58/11/114004. URL: https://doi.org/10.1088/0741-3335/58/11/114004.

[24] Robert S. Cohen, Lyman Spitzer, and Paul McR. Routly. “The Electrical Conductivity of an Ionized Gas”. In: *Phys. Rev.* 80 (2 Oct. 1950), pp. 230–238. DOI: 10.1103/PhysRev.80.230. URL: https://link.aps.org/doi/10.1103/PhysRev.80.230.

[25] V.M. Nakariakov and E. Verwichte. “Coronal Waves and Oscillations”. In: *Living Reviews in Solar Physics* 2.3 (1 2005). DOI: 10.12942/lrsp-2005-3. URL: https://link.springer.com/article/10.12942/lrsp-2005-3.

[26] M. Maraschek et al. “Observation of Toroidicity-Induced Alfvén Eigenmodes in Ohmically Heated Plasmas by Drift Wave Excitation”. In: *Phys. Rev. Lett.* 79 (21 Nov. 1997), pp. 4186–4189. DOI: 10.1103/PhysRevLett.79.4186. URL: https://link.aps.org/doi/10.1103/PhysRevLett.79.4186.

[27] Felix Klossek. “Charakterisierung des frequenzabhängigen Antwortverhaltens von magnetischen Messungen an ASDEX Upgrade”. bachelor thesis. LMU München, 2017.

[28] R C Isler. “A Review of Charge-Exchange Spectroscopy and Applications to Fusion Plasmas”. In: *Physica Scripta* 35.5 (May 1987), pp. 650–661. DOI: 10.1088/0031-8949/35/5/007. URL: https://doi.org/10.1088/0031-8949/35/5/007.

[29] B. Kurzan and H. D. Murmann. “Edge and core Thomson scattering systems and their calibration on the ASDEX Upgrade tokamak”. In: *Review of Scientific Instruments* 82.10 (2011), p. 103501. DOI: 10.1063/1.3643771. eprint: https://doi.org/10.1063/1.3643771. URL: https://doi.org/10.1063/1.3643771.

[30] Arne Kallenbach. “Multi-machine comparisons of divertor heat flux mitigation by radiative cooling with nitrogen”. In: *24th Fusion Energy Conference* (2012). URL: http://www-naweb.iaea.org/napc/physics/FEC/FEC2012/papers/345_ITRP128.pdf.

[31] S K Rathgeber et al. “Estimation of edge electron temperature profiles via forward modelling of the electron cyclotron radiation transport at ASDEX Upgrade”. In: *Plasma Physics and Controlled Fusion* 55.2 (Dec. 2012), p. 025004. DOI: 10.1088/0741-3335/55/2/025004. URL: https://doi.org/10.1088/0741-3335/55/2/025004.

[32] Fischer, Rainer. *IDA shotfile: Electron profiles*. URL: `https://www.aug.ipp.mpg.de/foswiki/bin/view/IDA/IDAElectronProfiles` (visited on 07/29/2021).

[33] Fischer, Rainer. *IDE equilibrium*. URL: `https://www.aug.ipp.mpg.de/foswiki/bin/view/IDA/IDE_Equilibrium` (visited on 07/25/2021).

[34] Tardini, Giovanni. *manuals/map_equ*. URL: `https://www.aug.ipp.mpg.de/aug/manuals/map_equ/` (visited on 07/25/2021).

[35] D.R. Hatch et al. "Microtearing modes as the source of magnetic fluctuations in the JET pedestal". In: 61.3 (Feb. 2021), p. 036015. DOI: `10.1088/1741-4326/abd21a`. URL: `https://doi.org/10.1088/1741-4326/abd21a`.

[36] E. Viezzer et al. "Evidence for the neoclassical nature of the radial electric field in the edge transport barrier of ASDEX Upgrade". In: 54.1 (Dec. 2013), p. 012003. DOI: `10.1088/0029-5515/54/1/012003`. URL: `https://doi.org/10.1088/0029-5515/54/1/012003`.

[37] A.O. Nelson et al. "Time-dependent experimental identification of inter-ELM microtearing modes in the tokamak edge on DIII-D". In: *Nuclear Fusion* 61.11 (Oct. 2021), p. 116038. DOI: `10.1088/1741-4326/ac27ca`. URL: `https://doi.org/10.1088/1741-4326/ac27ca`.

Danksagung

Das Ende dieser Arbeit ist der richtige Zeitpunkt, um einigen Menschen zu danken. Schließlich ist es nicht nur der Abschluss eines Projektes, sondern meines ganzen Studiums und einer Lebensphase.

Liebe Lisl, danke für deine Begleitung durch die gesamte Arbeit. Danke für deine Geduld und Zeit in unseren wöchentlichen Meetings, mit denen du mich durch den Schreibprozess geführt hast. Du hast mir wahnsinnig viel beigebracht und mich für die Forschung motiviert. Ich hoffe, dass noch viele Studenten in Zukunft diese Freude haben werden.

Meinen lieben Dank an das gesamte ASDEX Upgrade Team für die Zusammenarbeit. Ich habe immer ein Klima der Hilfsbereitschaft ohne Eigensinn gespürt, an dem ich mir ein Beispiel genommen habe. Das halte ich besonders in der Wissenschaft für unschätzbar wertvoll. Besonderen Dank an meine Kollegen Lidija und Georg, die von der TU Wien aus einen ähnlichen Weg wie ich gewählt haben und mir ein motivierendes Beispiel waren.

Danke an Fritz Aumayr für die akademische Betreuung meiner Arbeit und auch die Begleitung während vergangener Arbeiten. Es war mir eine große Hilfe, auch vor Ort in Wien Ansprechpartner zu haben und Teil eines Teams sein zu können.

Liebe Eltern, wie immer danke für eure Unterstützung, aber das zu sagen ist nicht genug. Ich danke euch für die Möglichkeit, meinen eigenen Wünschen nachzugehen. Viel wichtiger ist mir aber, dass ihr an mich glaubt. Jetzt könnt ihr das Ergebnis sehen und das freut mich besonders. Natürlich wird sich mit diesem Abschluss für uns einiges ändern und ich weiß selbst nicht genau, was die Zukunft bringt. Ich freue mich aber jetzt schon auf das nächste Mal nach Hause zu kommen, wie immer.